How do ancient mass-transport complexes influence subsequent failure events? A case study from the Kangaroo Syncline, offshore NW Australia

Nan Wu[1*], Christopher A.-L. Jackson[2], David M. Hodgson[3], Harya D. Nugraha[4,5], Guangfa Zhong[1]

[1]State Key Laboratory of Marine Geology, Tongji University, 1239 Siping Road, Shanghai, 200092, China
[2]Department of Earth Science and Engineering, Imperial College, Prince Consort Road, London, SW7 2BP, UK
[3]School of Earth and Environment, University of Leeds, Leeds, LS2 9JT, UK
[4]Center for Sustainable Geoscience, Universitas Pertamina, Jakarta, 12220, Indonesia
[5]Department of Earth Science, University of Bergen, Allégaten 41, N-5007 Bergen, Norway
*nanwu@tongji.edu.cn

Abstract

Mass-transport complexes (MTCs) are common features in all continental margins. In some passive margins, accumulations of stacked MTCs indicate repeated slope failure, which raises the question of whether MTC emplacement may influence or even pre-condition, subsequent slope failures. Here, we use 3D seismic reflection data from the Kangaroo Syncline, NW Australia, to investigate how pre-existing MTCs can prime subsequent failure events. We show that: i) lithological heterogeneity present within a sedimentary succession due to MTC emplacement can dictate where subsequent slope failure occurs; ii) relief along the top surface of an MTC controls the transport pathway and stratigraphic architecture of a subsequent MTC; iii) topography created by a buried MTC can enhance the erosive ability of subsequent slope failure events; iv) pre-existing MTCs headwall scarp can drive a cascading effect and influence multiple subsequent slope failures; and v) the thickness distribution pattern of buried MTCs could provide a mechanism for predicting the depocentre of future slope failure events. Buried MTCs have profound effects on the location, nature, geometry, and hazard potential of future slope failures. Therefore, investigating the interaction between multi-stacked MTCs has significant implications for geohazard impact assessment.

Keywords: Mass-transport complexes (MTCs), Exmouth Plateau, Geohazard assessment, Subaqueous slope failure, Subaqueous landsliding

1. Introduction

The term 'mass-transport complex' (MTC) is applied to a range of gravity-driven, subaqueous deposits resulting from creep, slide, slump, and debris flow processes (e.g. Dott Jr, 1963; Nardin et al., 1979; Nemec, 1990; Posamentier and Martinsen, 2011). MTCs can be very large (>10,000 km^3) and can travel quickly (>50 km/h) and long distances (i.e., >100 km), transporting large volumes of sediment, carbon, and nutrients from continental margins to the deep ocean (e.g., Talling et al., 2014; Kioka et al., 2019). The passage of an MTC can pose a great risk to submarine infrastructures (i.e. hydrocarbon- and windfarm-related platforms, and seabed cables), and generate powerful tsunamis that impact submarine ecosystems and threaten coastal populations (Harbitz et al., 2014; Talling et al., 2014; Lintern et al., 2019; Watkinson and Hall, 2019). The volumetrically largest MTCs on the planet have occurred on passive margins (Masson et al., 2006). However, these giant MTCs are hard to predict, as they are primed and triggered by interacting factors including sea level fluctuations, climate change, substrate character and heterogeneity, sediment supply rates, and tectonic activity (Masson et al., 2010).

In some passive margins, slope failures are frequent, leading MTCs to be the most volumetrically dominant component of basin-fills, where 50%-90% of a succession comprises stacked MTCs (Appendix 1; Solheim et al., 2005; Sawyer et al., 2009; Li et al., 2015; Reis et al., 2016; Nugraha et al., 2018; Omeru and Cartwright, 2019; Steventon et al., 2019; Barrett et al., 2021). The morphology, distribution, kinematic indicators, and preconditioning and trigger mechanisms of some volumetrically significant single MTCs have been considered. For example, the Storegga Slide (i.e. Kvalstad et al., 2005), the Baiyun Slide (i.e. Sun et al., 2018), the Gorgon Slide (i.e. Nugraha et al., 2022), and the Amapá Megaslide Complex and Pará-Maranhão Megaslide Complex (i.e. Reis et al., 2016), have been thoroughly examined. However, limited studies have investigated how pre-existing MTCs influence subsequent slope failures in successions with stacked MTCs (Masson et al., 2006). Thus, the role of the pre-existing MTCs in pre-conditioning the distribution, scale, and flow rheology and direction of subsequent slope failures remains understudied. Here, we investigate the dynamic interactions between six, post-Late Miocene MTCs imaged in high-resolution 3D seismic reflection volume from the Kangaroo Syncline, offshore NW Australia. We address the following key questions: (i) why are MTCs abundant in the Kangaroo Syncline? (ii) what is the role of pre-existing MTCs in preconditioning the location, thickness, and volume of material removed, transported, and deposited following future slope failures? And (iii) how do pre-existing MTCs influence the transport direction of the subsequent MTCs?

2. Geological setting

The Kangaroo Syncline (or Trough) is a sub-basin of the North Carnarvon Basin, located on the NW Australian continental margin (Figure 1A; Hengesh et al., 2013; Scarselli et al., 2013). As its name suggests, the Kangaroo Syncline is a c. 100 km wide synclinal depocentre, trending NNE-SSW, being defined by a relatively low (0.08°-1.5°) seabed gradient (Hengesh et al., 2013). It is several hundred kilometres long and tens of kilometres wide, with present water depths of 1000-1300 m (Figure 1A; Exon et al., 1992; Hengesh et al., 2013). The Kangaroo Syncline formed in response to several rifting events that most recently occurred between the Late Jurassic and Early Cretaceous (Longley et al., 2002). During the Late Cretaceous, uplift of the Australian continental hinterland and structural inversion offshore on the southern Exmouth Plateau led to the formation of the Kangaroo Syncline and Exmouth Plateau Arch (Tindale et al., 1998). During the Late Oligocene, the Kangaroo Syncline and the Exmouth Plateau Arch were reactivated due to the collision of the Australian and Eurasian plates (Barber, 1988; Keep et al., 1998; Cathro and Karner, 2006). During the Late Miocene, the collision of the Australian Plate with the Eurasia and Pacific plates led to further growth and deepening, respectively, of the Exmouth Plateau Arch and Kangaroo Syncline (Tindale et al., 1998). From the Late Miocene to the Present, continuous collision of the Australian Plate with the Eurasia Plate accelerated tectonic subsidence of the Kangaroo Syncline and inverted faults beneath the present continental shelf (Hull and Griffiths, 2002).

This study focuses on the late passive margin megasequence (Late Miocene to Present). Water depths at this time were bathyal (800-1500 m), with deposition dominated by eupelagic carbonate (Exon et al., 1992; Haq et al., 1992). The study interval lies between Horizon H0 (approximately Late Miocene) to the seabed (Figures 1B, 1C). Ocean Drilling Program (ODP) site 762 lies c. 270 km east of the study area (Figure 1A), near the apex of the Exmouth Plateau Arch. Core and geotechnical data from ODP site 762 indicate that the study interval is dominated by highly compressible, low-velocity, water- and foraminifera-rich, carbonate oozes (Figure 1B; Haq et al., 1992; Wu et al., 2023).

3. Dataset and methods

The primary dataset used in this study is the Willem 3D seismic reflection survey, acquired in 2011 (Figures 1A, 1D). It covers a c. 2628 km^2 area of the lower continental slope and adjacent depocentre (i.e. the Kangaroo Syncline), in water depths of 200-1500 m (Figure 1A). The 3D seismic reflection data were post-stack time-migrated (PSTM) and are displayed using SEG reverse polarity, where a downward increase and decrease in acoustic impedance are expressed as blue/black (negative) and red/white (positive) reflection events, respectively. The sampling rate of the seismic reflection data is 2 ms, and the bin size of the seismic survey is 25 x 25 m. From the seabed to the study interval, the dominant frequency of the 3D seismic reflection data decreases from ca. 60 Hz to ca. 40 Hz, and the average seismic velocity increases from 1750 m/s to 2000 m/s; we therefore estimate an approximate vertical resolution of 7.3 m at the seabed, decreasing to 12.5 m near the base of the studied interval. The excellent spatial resolution of the 3D seismic reflection data allows a detailed interpretation and characterization of the MTCs' geometries and emplacement directions.

The interval of interest (Late Miocene – Recent; Figures 1B, 1C) correlates to seismic unit 3 of Nugraha et al. (2018) and seismic unit 2 of Wu et al. (2023), who studied the seismic-stratigraphy of adjacent areas. Previous studies indicate that the interval of interest contains MTCs that either originated from the bathymetric highs of the lower NW Australian continental slope, or the upper slope of the Exmouth Plateau Arch (Hengesh et al., 2012; Scarselli et al., 2013; Nugraha et al., 2018). Eleven seismic horizons (H0 to the seabed) have been interpreted to define the base and top of each MTC, based on vertical and lateral changes in seismic facies, the packages they define, and the expression of their bounding surfaces (Figures 2A, 2B). Variance and amplitude contrast attributes have been extracted from the basal shear surface and the top surface of MTCs to identify kinematic indicators that may reveal the MTC emplacement direction and emplacement-related deformation. The variance attribute calculates the variability of a trace to its neighbour over a particular sample interval and produces interpretable lateral changes in acoustic impedance (Van Bemmel and Pepper, 2000). The amplitude contrast attribute calculates the spatial gradient on an image; it improves the edge detection spatially and thereby helps the identification of the terminations of the discontinuities (Aqrawi and Bø, 2016). Isochron (i.e. time-thickness) maps of each MTC are computed from their basal and upper surfaces, with these being used to assess the spatial relationships between subsequent MTCs. The width and depth of grooves are calculated to quantify the erosional ability of MTCs.

4. Results

This study focuses on six stacked MTCs (MTC 1-6) that comprise nearly 80% of the stratigraphic thickness of the studied stratigraphic interval (Figures 2A, 2B). In addition to the six studied MTCs, three younger MTCs are also observed at shallower depths referred to as undifferentiated MTCs (Figure 2B). These younger MTCs were not investigated due to their limited areal extent and do not erode into the underlying MTCs. The six studied MTCs are characterised by packages of chaotic, variable amplitude reflections (Bull et al., 2009; Posamentier and Martinsen, 2011). They are bound below by a positive polarity, high amplitude, continuous basal shear surfaces, and above by a medium amplitude and, negative polarity, rugose top surface (Figure 2A). In the following section, we describe the distribution, and external and internal geometry, and interpret their emplacement direction and mechanics, in stratigraphic order from oldest (MTC-1) to youngest (MTC-6).

4.1 MTC-1

Description: MTC-1 is internally seismically chaotic and defined at its base and top by H1 and H2, respectively (Figures 3A, 3B, 3C). A variance attribute calculated within H1 indicates a tongue-shaped geometry, narrowing to the NNE (Figures 3A, 3B). The eastern boundary of MTC-1 is defined by an N-S trending erosional margin associated with an undifferentiated MTC, whereas its western boundary trends NE-SW and is defined by the lateral (erosional) margin of the younger MTC-2 (Figure 3B). Within MTC-1, NNW-SSE trending lateral ramps and E-W trending internal ramps are presented in the middle, and numerous NNE-SSW trending, diverging lineations are observed beyond the internal ramp (Figure 3B). In the seismic dip section, the MTC-1 thins to the northeast, and its basal shear surface dips downward to the NNE (Figure 3D).

Interpretation: In part, the geometry of MTC-1 is an erosional remnant due to the later incision by MTC-2 (i.e. in the west) and an undifferentiated MTC (i.e. in the east) (Figure 3B) and was more extensive towards the west and east. The lineations developed beyond the internal ramp are interpreted as basal grooves (i.e. Posamentier and Martinsen, 2011; Sobiesiak et al., 2018), formed by clasts carried within the host flows that scoured the contemporaneous seabed. Grooves typically form parallel to the MTC transport direction, together with the NNE-SSW downward trending of the basal shear surface, suggesting MTC-1 was emplaced towards the NNE (Bull et al., 2009). Internal and lateral ramps result from MTCs cutting up through stratigraphic levels, creating a step-like geometry in cross-section (Frey-Martínez et al., 2006; Bull et al., 2009). The lateral ramp is considered parallel to the MTCs' transport direction, whereas the internal ramp is perpendicular to the MTCs' emplacement direction (Bull et al., 2009). Therefore, we interpret a NNE translation direction for MTC-1, consistent with that inferred from the grooves (Figure 3B).

4.2 MTC-2

Description: MTC-2 is defined at its base by H3 and its top by H4 (Figures 2A, 2B). A variance attribute calculated within H3 indicates MTC-2 has a semi-elliptic geometry, with its eastern boundary defined by a NE-SW trending headwall scarp and its western boundary by an erosional ramp associated with the younger MTC-3 (Figures 4A, 4B). The isochron of MTC-2 reveals it thins westward from its headwall (Figure 4C). The variance attribute indicates that MTC-2 contains numerous parallel to sub-parallel, block-shaped packages in its eastern part (Figures 4A, 4B). In seismic cross sections, these form ridge-shaped blocks flanked by troughs (Figure 4D). Typical dimensions of the blocks are 210-300 m high, 170-210 wide, and 800-1,200 m long, with minor internal deformation (Figure 3C, 4D). The intervening troughs are 160–260 m deep, 190–230 m wide, 800–1,200 m long and are defined by a chaotic, variable-amplitude seismic facies (Figure 4D). The lower section of the blocks is characterized by chaotic seismic facies, comparable in expression and thickness to MTC-1 (Figure 3C, 4D). The chaotic seismic facies are also bound by medium to high-amplitude, positive reflections, comparable to those bounding MTC-1 (Figure 3C). The blocks decrease in size and lose their block-shaped form and become internally disaggregated westwards (Figure 4D).

Interpretation: MTC-2 was previously described by Wu et al. (2021b), who document a c. 300 m thick succession of undeformed slope strata between MTC-1 and MTC-2 (Figure 4D). Unlike MTC-1, the basal shear surface of MTC-2 lacks kinematic features (i.e. lateral margins, ramps, or grooves; Figure 4A) that record its emplacement direction. Wu et al. (2021b) interpreted an overall north-northwestward translation direction, along the axis of the Kangaroo Syncline, based on its headwall scarp orientation (i.e., NE-SW) and trend in block size (i.e. blocks decrease in size towards the WNW) (Figure 4B; Wu et al., 2021b). The intra-MTC blocks are interpreted as being related to lateral spreads based on their geometric characteristics and distribution. The similarity in the seismic facies succession characterising the intra-MTC blocks and the undeformed strata (i.e. a thin MTC overlain by largely undeformed strata) suggests the former are derived from the latter (Figures 3C, 4D). This is supported by the blocks in the eastern part of MTC 2 being the same thickness as the laterally adjacent, largely undeformed interval (Figures 3C). We therefore interpret the emplacement of MTC-2 can dislocate underlying deposited MTC-1, and segments of deposited MTC-1 have formed the basal shear zone of younger MTC-2.

4.3 MTC-3

Description: MTC-3 overlies MTC-2, separated by a thin (c. 30 m) package of slope deposits and it is bounded by H4 at its base and by H5 at its top (Figures 2A, 2B). The variance attribute calculated from H4 reveals that MTC-3 has a scallop-shaped geometry in plan-view (Figures 5A, 5B). The eastern boundary of MTC-3 is defined by an NNE-SSW trending scarp, whereas its western boundary is beyond the 3D seismic reflection dataset (Figure 5B). The isochron of MTC-3 shows that it thins eastward, showing an opposing thickness trend to MTC-2 (Figure 5C). A seismic section through MTC-3 reveals that it comprises blocky seismic facies in the west, chaotic seismic facies near its centre, and semi-continuous, medium-amplitude seismic reflections offset by thrusts faults in the east (Figure 4D). The central region of MTC-3 contains several E-W to SE-NW trending linear features that are least 7 km long (Figures 5A, 5B). A seismic section shows that in cross-section the linear features have a U-shaped geometry that truncate underlying reflectors with scales up to 400 m wide and 60 m deep (Figure 5D). The eastern region contains numerous broadly eastward-convex, regularly spaced undulations, with the eastern, most distal part of MTC-3 notably coinciding with where the underlying lateral spreads (associated with MTC-2) are developed (Figures 5B, 5E). In detail, the regularly spaced undulations are characterised by semi-continuous, medium-amplitude seismic facies that terminate against the relief created by the underlying lateral spreads (Figure 5E). Further east, the seismic reflections are continuous and drape the lateral spreads, defining low-relief folds (see insert figure in Figure 5E).

Interpretation: The NNE-SSW trending eastern boundary is interpreted as the distal limit of MTC-3, where the deposit changes from principally debritic material to undeformed, slope sediments (Figures 5A, 5B). The linear features in the west of the seismic survey are interpreted as erosional scours (i.e. Moscardelli et al., 2006), which potentially formed by the sliding or dragging of blocks across the substrate (Gee et al., 2005; Sobiesiak et al., 2018). The regularly spaced undulations developed near the eastern boundary of MTC-3 are interpreted as pressure ridges caused by compression or horizontal shortening of transported material, noting that such features are normally convex in the downslope direction (Nissen et al., 1999; Bull et al., 2009). The pressure ridges are underlain by, and likely genetically related to, thrusts, suggesting the failed mass remained frontally confined (Figure 5E; Frey-Martínez et al., 2006). Pressure ridges and scours normally develop perpendicular and parallel to the MTCs' main flow direction, respectively (Bull et al., 2009). We therefore interpret that the gross transport direction of MTC-3 was eastward to southeastward (Figure 5B).

The lateral spreads associated with MTC-2 developed considerable positive relief of a few tens of metres overall several kilometres horizontally; we infer this relief caused shortening and thrusting in the distal part of MTC-3 (see the zoom-in section in Figure 5E). MTC-2 and MTC-3 show opposing emplacement directions and thickness trends (Figures 4C, 5C), suggesting that relief associated with the former controlled the bathymetric template onto which the latter was emplaced. After deposition of MTC-3, the paleo-seabed began to heal via the deposition of fine-grained carbonate oozes that drape the top surface of MTC-3 (Figure 5E; Nugraha et al., 2018).

4.4 MTC-4

Description: MTC-4 is separated from MTC-3 by a 30-70 m thick package of slope deposits and is bounded by H7 at its base and by H8 at its top (Figures 2A, 2B). The amplitude contrast attribute extracted from H7 reveals that MTC-4 has a lobe-shaped geometry in plan-view, with NW-SE trending lateral margins (Figures 6A, 6B). The isochron of MTC-4 shows it is thinnest in its middle and thickest in its western and eastern portions (Figure 6C). Curvilinear striations are observed on the basal shear surface in the eastern and western regions of the MTC-4 (Figures 6A, 6B). These striations are 20-40 km long and sub-parallel. In seismic cross-section, the striations are erosional, defining a prominent V-shaped geometry, 12-50 ms deep and 50-300 m wide (Figure 6D). In its north-western portion (where it caps MTC-3), MTC-4 is locally thick where the underlying MTC-3 is thin, and vice versa (Figures 6C, 6D). In the same area, we observe a NW-SE trending lineation on the basal shear surface that is superimposed above the headwall scarp of the buried MTC-2 (Figures 6B, 6D). The NW-SE trending lineation separates the striations with two different populations along the BBS of MTC-4 (Figures 7A, 7B). For example, outside (SE) the lineation they trend NW-SE to NNW-SSE (315-330^{o}), whereas inside (NW) the lineation they trend NNE-SSW to NE-SW (015-045^{o}), broadly parallel to the axis of the Kangaroo syncline (Figures 7C). To assess how erosion varies between the NW-SE trending lineation, we pick one of the most continuous striations (G-1; Figure 7B) to quantify down-trend variations in its width and depth. From the outside to inside the lineation, the width and erosion depth of the G-1 increased sharply from 110 to 270 m and 18 to 45 ms, respectively (Figure 7D).

Interpretation: Similar to those in MTC-1, the curvilinear striations are interpreted as grooves formed due to erosion (Posamentier and Kolla, 2003; Gee et al., 2005). The NW-SE trending lineation developed in the NW portion of MTC-4 is interpreted as an internal ramp, where MTC-4 cut down into the deeper stratigraphy (Figures 6B, 6D; Bull et al., 2009). The bathymetric contrast between the internal ramp reflects un-healed relief above MTC-3, which initially formed immediately downdip of the headwall scarp associated with MTC-2 (Figure 6D). The groove trend suggest MTC-4 was steered away from a shallower area (outside the lineation) and cuts down to be more confined (inside the lineation; i.e. Figure 7B). The grooves are wider and deep within the internal ramp suggesting increased erosion of the substrate reflected by the deeper incision on the BSS (Figure 7D). The increasing scale of grooves indicates that the erosive forces from the MTC-4 gouge into the substrate have increased when it debouches into the area influenced by the headwall scarp of underlying MTC-2. The thickness of MTC-4 thus increases in the area where MTC-2 is deposited, resulting in an internal ramp near the eastern boundary (i.e. headwall scarp) of the latter (Figures 6B, 6D). Therefore, we suggest that MTC-2 controlled local seabed topography that influenced the emplacement of MTC-4, enhancing its erosive ability, diverting its flow direction, and providing a focal point for its ultimate deposition.

4.5 MTC-5 & MTC-6

Description: MTC-5 directly overlies MTC-4, and is bounded by H9 and H10 at its base and top, respectively (Figures 2A, 2B). The amplitude contrast attribute calculated on H9 reveals that MTC-5 is the most aerially extensive in the study area (at least 2500 km^2; Figures 8A, 8B). The isochron of MTC-5 displays a tripartite thickness distribution, being thickest in the SW and NE portions and thinner in-between (Figure 8C). MTC-5 has an NW-SE trending scarp defining its updip margin that is located in the SE section, and several asymmetrical, sparsely distributed blocks just west of this feature (Figures 8A, 8B). The NW-SE trending scarp separates the internally deformed seismic facies from the undeformed substrate, the contact between the MTC and substrate is marked by a strong amplitude seismic reflection with positive polarity (Figure 8D).

In its central area, MTC-5 contains a large tabular-shaped block with a NW-SE trending long axis. The tabular-shaped block is c. 17 km along its long axis and c. 7 km across its short axis, and it is characterised by undeformed, continuous reflections that are sharply surrounded by chaotic seismic reflections characterising the main body of MTC-5 (Figure 8E). There is no visible basal deformation beneath the tabular-shaped block (Figure 8E). In the NE and western portions of MTC-5, several sinuous, NW-SE trending, 17-30 km-long lineations are observed (Figures 8A, 8B). The blocks within MTC-5 are c. 700 m long and c. 500 m wide, and internally folded and faulted, but still moderately laterally continuous seismic reflections (Figure 8D). The edges of the blocks are separated by steeply outward-dipping flanks (Figure 8D).

MTC-6, the youngest MTC overlies MTC-5, with its base and top defined by H10 and seabed, respectively (Figures 2A, 2B). MTC-6, broadly trends NW-SE and is confined to the NE part of the study area, has a tongue-shaped geometry that is defined by two distinct lobes in the NW (Figures 9A, 9B). The eastern and western boundaries of MTC-6 are characterized by NW-SE trending lateral margins (Figures 9A, 9B). The isochron of MTC-6 reveals it is thick in areas where the underlying MTC-5 is thin, and thin or absent where the underlying MTC-5 is thick (Figure 9C). The seismic section of MTC-6 consists of internally chaotic seismic facies that thins and pinches out toward the local topographic high associated with positive relief along the upper surface of MTC-5 (Figures 9D).

Interpretation: We interpret the lineations in MTC-5 as emplacement-related grooves and the scarp defining its SE margin as a headwall scarp. The location of the headwall scarp defines the source area of the slope failures (Bull et al., 2009; Posamentier and Martinsen, 2011); thus, given the headwall scarp of the MTC-5 is located on the lower continental slope, we infer it was sourced from here and transported northwestwards. This interpretation is consistent with the NW-SE trend of the basal grooves and the long axis direction of the remnant block (Figure 8B). The disrupted blocks developed near the headwall scarp are interpreted as transported blocks representing relatively competent pieces of failed material that have been transported within the MTC (Figure 8D; i.e. Frey Martinez et al., 2005; Bull et al., 2009). The internally undisturbed block is interpreted as remnant block of substrate surrounded by failed and transported material within the main MTC body (Figure 8E; i.e. Frey Martinez et al., 2005; Bull et al., 2009). The NW-SE trending margins associated with MTC-6 are interpreted as its lateral margins (Figures 9A, 9B). Based on the trending direction of its lateral margins, we interpret that MTC-6 was emplaced towards the NW. The offset nature of MTC-5 and MTC-6 suggests the relief of the former influenced deposition of the latter.

5. Discussion

We show that the post-Miocene succession of the Kangaroo Syncline is characterised by stacked MTCs. In this section we consider the potential controls on the relative abundance of MTCs in the Kangaroo Syncline, discuss how earlier MTCs can influence the location and scale of subsequent slope failures, and consider the implication of our results for predicting the future occurrence of MTCs and related geohazards and mitigating their impacts.

5.1 Why was MTC emplacement common in the Kangaroo Syncline in the Neogene?

MTCs in the Kangaroo Syncline form nearly 80% of the c. 600 m-thick Neogene section (Figures 2A, 2B). The repeated emplacement of MTCs indicates the Kangaroo Syncline has been a major depocenter for material originating from adjacent slope failures. Therefore, there is a substantial geohazard risk to valuable subaqueous infrastructures that are built or planned to be built in the Kangaroo Syncline (e.g., oil rigs and subsea gas trunk lines) (Piper et al., 1999; Hengesh et al., 2012; Gavey et al., 2017; Pope et al., 2017).

5.1.1 Carbonate oozes, sediment properties, and mass-failure

In the Kangaroo Syncline, carbonate ooze, consisting of fragile foraminifera and nannofossils, has and have been the dominant sediment deposit since the late Miocene (Nugraha et al., 2018). Carbonate oozes are highly compressible and have distinct geotechnical characteristics, including high water content (i.e. >50%), low permeability, and low shear strength compared to fine-grained siliciclastic sediments (von Rad, 1992; Urlaub et al., 2015; Gatter et al., 2021). The continuous deposition of carbonate oozes can result in sudden dewatering that causes an increase in sediment pore pressure, resulting in a sufficient excess pore pressure to precondition a low-gradient slope to fail (e.g. Tanaka and Locat, 1999; Volpi et al., 2003; Davies and Clark, 2006). Furthermore, the amount of water stored within shell chambers and skeletal pores in ooze can be as high as 15% of their dry weight (Palmer-Julson and Rack, 1992; Rack et al., 1993). The crushing of fragile biogenic particles could lead to further expulsion of intraparticle water, representing an additional source of pore pressure (Urlaub et al., 2015). Laboratory experiments suggest that carbonate oozes are more susceptible to failure than siliciclastic sediments (Gaudin and White, 2009). During the shear strength cyclic T-bar test of carbonate oozes and siliciclastic sediments, the residual shear strength of carbonate oozes drops rapidly to only 10% of their initial strength, whereas the residual strength of siliciclastic sediments can be up to 55% of their initial strength (Figure 10A; Gaudin and White, 2009). Consequently, carbonate oozes lose shear strength rapidly when their strain-bearing capacity is exceeded, which may explain why slope failures occur frequently in ooze-rich settings, even on very gently dipping slopes characterised by low rates of sediment accumulation, such as the Kangaroo Syncline.

5.1.2 The relationship between seismicity and sediment properties

Although the collision between the Australian and Eurasian plates has generated seismicity since the Late Miocene, the Exmouth Plateau is considered a relatively stable, low seismicity passive margin setting (Scarselli et al., 2013; Nugraha et al., 2018). The seismicity of an area can alter the initial (i.e., immediately post-depositional) sediment properties. For example, siliciclastic sediments within the first 100 m below the seabed that are exposed to repetitive low-magnitude earthquakes can progressively increase their shear strength through shear-induced compaction and dewatering (a process termed seismic strengthening; Sawyer and DeVore, 2015; Ten Brink et al., 2016). Therefore, siliciclastic sediments on active margins typically have higher undrained shear strength and can withstand higher static and dynamic shear stresses than sediments at equivalent depths on relatively aseismic passive margins (Figure 10B; Nelson et al., 2011; Sawyer and DeVore, 2015; Ten Brink et al., 2016). Conversely, when repetitive seismicity (thus the seismic strengthening process) is absent, sediments have lower shear strengths (Figure 10B) and are more susceptible to slope failures than those on active margins (i.e. Sawyer and DeVore, 2015; DeVore and Sawyer, 2016). The shear strength of the carbonate ooze in the Kangaroo Syncline ranges from 1.2 kPa to 12.5 kPa in shallow (i.e., <100 meters below seabed) sediments, which is at the lower end of the passive margin trend and does not show any evidence for seismic strengthening (i.e., the undrained shear strength is markedly lower than values characterising active margins; Figure 10B). Carbonate oozes in Kangaroo Syncline may thus be extremely unstable due to their extremely low shear strength.

5.1.3 Fluid venting system and vertical fluid migration

Excess pressures generated by fluid and/or gas migration are considered key primers for slope failures globally (Bünz et al., 2005; Berndt et al., 2012), with this also being true for the Kangaroo Syncline (Wu et al., 2023). In the latter case, excess pore pressure had, and possibly still has, two sources: 1) from silica diageneses (opal-A to opal-CT conversion) during the burial of the Eocene, chalk-rich succession (Wu et al., 2023) - a similar mechanism was proposed for a submarine landslide in the Faroe-Shetland Channel, NW offshore UK (Davies and Clark, 2006); and 2) gas was likely migrating from the hydrocarbon-bearing Mungaroo Formation (Triassic) (Paganoni et al., 2019; Velayatham et al., 2019) - a similar priming mechanism has been identified offshore Norway, in this case being associated with gas hydrate dissociation and migration behind the headwall of the Storegga Slide main headwall (Sultan et al., 2003; Strout and Tjelta, 2005). Therefore, sedimentary basins characterised by widespread, sustained, and more importantly, focused gas or fluid generation and migration pose higher risk of slope failure, such as in Kangaroo Syncline.

In summary, the abundance of MTCs in the Kangaroo Syncline can be attributed to the interplay of widespread and sustained carbonate ooze deposition, the absence of seismic strengthening processes, and the prevalence of vertical fluid migration.

5.2 How do pre-existing MTCs influence later slope failures?

This study shows that factors such as lithological and hydraulic heterogeneity, resulting from interactions between MTCs and their substrate, and relief above previously emplaced MTCs, influenced the distribution and stacking patterns of MTCs. Shear compaction of the substrate, generated by the passage of an MTC, can increase and decrease its density and permeability, respectively (Wu et al., 2021a). The basal shear surfaces of MTCs are generally more consolidated than lithologically comparable slope or basin-floor strata, showing high bulk density and shear strength, low porosity and permeability. Basal shear surfaces may therefore represent intra-stratal hydraulic boundaries, influencing or limiting fluid migration and the related distribution of overpressure, and thus the overall strength profile of the sedimentary succession (Wu et al., 2021a).

In the Kangaroo Syncline, prior to the emplacement of MTC-2, the basal shear surface of MTC-1 may have represented a hydraulic boundary between the overlying c. 300 m thick carbonate ooze-bearing sequence, and the underlying carbonate ooze-dominated substrate (Figure 11A). This surface may have permitted the build-up of excess pore pressure and generation of weak layers within the substrate, ultimately priming slope failure and the formation and emplacement of MTC-2 (Figures 11A, 11B). The emplacement of MTCs, and more specifically processes related to the development of their basal shear surfaces, can result in the formation of intra-stratal hydraulic boundaries that prime subsequent slope failures, ultimately defining the extent of the basal failure zone and ultimate volume of subsequent MTCs.

MTC emplacement can remould the submarine seascape, creating giant, scarp-bound seabed depressions that cover thousands of square kilometres, and that change the slope profile, potentially making future failures more likely (i.e. Kneller et al., 2016). Previous studies suggest that relief above MTCs influence sediment transport pathways by diverting subsequent turbidity currents (Hansen et al., 2013; Ortiz-Karpf et al., 2015; Corella et al., 2016; Ward et al., 2018; Wu et al., 2022), or by disrupting the equilibrium condition of subsequent along-shelf transported ocean currents and facilitating their transformation into down-slope transported gravity flows (Wu et al., 2024), or by generating ponded accommodation within which (turbidity current-fed) lobes and contourite channels are deposited (Solheim et al., 2005; Olafiranye et al., 2013; Li et al., 2015; Kneller et al., 2016) (see Appendix-2 for details). However, the way in which pre-existing MTCs control the flow direction, depositional pattern, and stratigraphic architecture of subsequent failures has received less attention.

In the Kangaroo Syncline, we show that the large blocks (c. 300 m in height) within MTC-2 formed substantial relief (i.e., >100 m and that extends 10's of km laterally) on the contemporaneous seabed (Figure 11B). This relief controlled the down-dip extent and style of strain within MTC-3, with shortening and thrusting occurring where it impinges on this relief (bathymetrical control; Figures 11C). Whereas MTC-3 largely healed the accommodation created by failure of slope material comprising MTC-2, some accommodation remained between blocks within MTC-2 (Figure 11C). The remaining accommodation above MTC-3 contributed to the bathymetrical partitioning of MTC-4 (Figure 11D). Slope breaks formed by relief along MTC-2 are expressed within the basal shear surface of MTC-4, evident as the relief of MTC-4's basal shear surface is lower immediately adjacent to the location near the headwall scarp of MTC-2 (Figure 11D). This indicates the former controlled the emplacement direction and erosional capacity of the latter. Relief associated with pre-existing MTCs can therefore influence the emplacement, distribution, and erosional capacity of subsequent MTCs. Since the main energy of the tsunami waves travel in the direction of slope failure motion, the failure direction is as important as the speed and scale of movement (Driscoll et al., 2000; Schnyder et al., 2016). We suggest that conducting subsurface and surface mapping of MTC top surfaces, particularly at locations where large blocks and scarps exist, could help in predict future slope failure routes and potential danger zones (i.e., pathways for subsequent failure processes), thereby reducing risks for seabed infrastructure.

Slope failure is often associated with formation of large evacuation zones and steep headwall scarps (e.g., Solheim et al., 2005; Nugraha et al., 2022). In the Kangaroo Syncline, the initiation of MTC-2 created a large evacuation zone characterised by >200 m of vertical relief and a c. 30 km long, NNE-SSW oriented headwall scarp (Figure 12A). This headwall scarp separated the paleo-seabed into bathymetrically high and low areas in the east and west, respectively (Figure 12A). This feature subsequently influenced the relief associated with the basal shear surface of younger MTCs (Figures 12B-D). For example, the relief calculated on the basal shear surfaces of subsequent MTC-4 and MTC-5 dip sharply near the location of MTC-2's headwall scarp (Figures 12C, 12D). The headwall scarp associated with MTC-2 also influenced the thickness distribution of subsequent MTCs. For example, MTC-4 and MTC-5 are thicker in the low area immediately adjacent to the headwall scarp of the MTC-2 (Figure 13). The headwall scarp of pre-existing MTC-2 may therefore control seabed relief and local thickness changes in younger MTCs for a relatively long time after initial formation.

In the Kangaroo Syncline, the spatial distribution of younger MTCs is often bound by the local topographic highs created by pre-existing MTCs, with their boundaries coinciding with areas where pre-existing MTCs are locally thickest (i.e., MTC-2 vs MTC-3; MTC-5 vs MTC-6; Figure 13). We show that in areas where pre-existing MTCs are relatively thick, subsequent MTCs are relatively thin, and vice versa. We note the emplacement of a younger MTC may erode the pre-existing MTCs, modifying their original thickness distribution. However, because gravity-driven slope failures are sensitive to variations in slope gradient, they are preferentially accommodated in bathymetrically low regions (Kneller et al., 2016). We therefore suggest that the buried MTCs can exert a primary control on the thickness distribution of subsequent slope failures. Detailed mapping of MTCs is therefore essential in slope failure-prone areas, noting that future subsea construction should avoid areas where seabed MTCs are relatively thin, given this may represent the depocentre for a future MTC (Figure 13).

6. Conclusions

Our study provides a valuable case study on the dynamic interactions and influence between stacked MTCs and enables a better understanding of slope failure mechanisms in passive margins globally. Based on the results of this study, the following conclusions can be drawn:

(1) We reveal that the Kangaroo Syncline accommodate at least six large stacked MTCs that comprise nearly 80% of the total stratigraphy. We suggest that the Kangaroo Syncline is particularly prone to slope failure because of the interplay of three factors: widespread and sustained carbonate ooze deposition, the lack of seismic strengthening process, and the abundance of vertical fluid migration.

(2) We demonstrate that pre-existing MTCs can have far-reaching effects on the stability of the surrounding sediment pile. Potentially, MTC emplacement can trigger a headwall scarp effect that influences the bathymetry and distribution of subsequent slope failures. More specifically, pre-existing MTCs can affect lithology composition, provide bathymetric constraints to failure displacement, switch direction with the flow, and enhance the erosion capacity of the subsequent slope failures.

(3) Our results demonstrate that buried MTCs exert a significant influence on subsequent slope failure distribution patterns and their depocentre. Therefore, measuring the pre-existing MTCs (especially their top surface) provides a unique analogue for predicting future MTC locations and providing key information for the planning of future seabed infrastructure and hazards mitigation.

Figure Caption

Figure 1. (A) The bathymetric map of the NW Australian region shows the study area location, key tectonic structures, and location of datasets. The location of ODP 762 is marked as a red dot, the Willem 3D seismic is indicated by a red polygon and the 2D seismic data by a solid grey line. (B) Tectonostratigraphic chart for the study area, lithology and age is defined in the ODP 762 report. All data relating to the ODP log is depth below the seabed from ODP site 762. (C) Regional seismic cross-section through the Exmouth Plateau Arch, Kangaroo Syncline and the lower continental slope. Horizon H0 is the base of the study interval and has been tied to the Late Miocene Unconformity surface. H0 is equivalent to Reflector 7 of Boyd et al. (1993), N17–1 horizon of Hull and Griffiths (2002), Horizon C of Nugraha et al. (2018), and Horizon H2 of Wu et al. (2023). See Figure 1A for the location of Figure 1C. (D) Zoomed in view of Willem 3D polygon, illustrating the location of the figure demonstrated in this study.

Figure 2. (A) The regional seismic cross-section through the Willem 3D shows the study interval and the late Miocene Unconformity surface (H0). (B) Sketches showing the location of stacked MTCs 1-6, undifferentiated MTCs and key seismic horizons (H1-seabed). See Figure 1D for location.

Figure 3. (A) Variance attribute map calculated on the basal shear surface of MTC-1, showing the boundaries and internal key structures of the MTC-1. (B) Interpreted sketch of MTC-1, showing the boundaries and internal key structures of the MTC-1. (C) The seismic section cutting through MTC-1 and MTC-2 shows the detailed structures and seismic characters. (D) The seismic section cutting along the transport direction of MTC-1. See Figure 3B for location.

Figure 4. (A) Uninterpreted variance attribute map calculated on the basal shear surface of MTC-2, showing the boundaries and internal key structures of the MTC-2. (B) Interpreted sketch of MTC-2, showing the MTC boundaries, key kinematic indicators and the transport

direction. (C) Isochron (TWT thickness) map of MTC-2, indicating a westward thickness thinning trend. The contour interval is 60 ms. (D) The seismic section cutting through MTC-2 and MTC-3 shows the detailed structures and seismic characters. See the location of this seismic section in Figure 4B.

Figure 5. (A) Uninterpreted variance attribute map calculated on the basal shear surface of MTC-3, showing the boundaries and internal key structures of the MTC-3. (B) Interpreted sketch of MTC-3, showing its boundaries and key kinematic indicators. (C) Isochron (TWT thickness) map of MTC-3, indicating an eastward thickness thinning trend. The contour interval is 60 ms. (D) The seismic section cuts through the eastern margin of MTC-3, showing the thrust terminating against the underlying spread blocks. (E) The seismic section cuts through the scours of MTC-3, showing the cross-sectional profile of the scours. See the location of the seismic sections in Figure 5B.

Figure 6. (A) The uninterpreted variance attribute map calculated on the basal shear surface (H7) of MTC-4 shows the MTC's boundaries and internal key structures. (B) Interpreted sketch of MTC-4, showing the MTCs boundaries and key kinematic indicators. (C) Isochron (TWT thickness) map of MTC-4, the contours are every 60 ms. (D) Seismic section cutting through MTC-4 shows the relief variation near the headwall scarp of MTC-2 and groove details. See the location of the seismic section in Figure 6B.

Figure 7. (A) Zoom-in map of Figure 6A. (B) The interpreted map of Figure 6A shows the grooves developed on the MTC-4's basal shear surface. (C) The Rose diagram shows the orientation of the grooves, blue indicates grooves developed outside the NW-SE trending lineation, and pink indicates grooves developed within the NW-SE trending lineation. (D) The width and incision depth of groove G-1, see the location of groove G-1 in Figure 7B.

Figure 8. (A) Uninterpreted variance attribute map calculated on the basal shear surface (H9) of MTC-5, showing the boundaries and internal key structures of the MTC-5. (B) Interpreted sketch of MTC-5, showing the boundaries, headwall scarp, internal blocks and other kinematic indicators of this MTC. (C) Isochron (TWT thickness) map of MTC-5, revealing a thick-thin-thick tripartite pattern. (D) The seismic section crosses the area of the headwall scarp and translated blocks of the MTC-5. Note the basal shear surface's step-shaped geometry near the headwall. (E) The seismic section along the MTC-5 remnant blocks. See the location of these seismic sections in Figure 8B.

Figure 9. (A) The variance attribute map calculated on the basal shear surface (H10) of MTC-6 shows the MTC's boundaries and internal key structures. (B) Interpreted sketch of MTC-6, showing the boundaries and lateral margins of the MTC-6. (C) Isochron (TWT thickness) map of MTC-6, showing the depocentre of the MTC-6. (D) Seismic cross section cutting across the MTC-6, showing the thickness of this MTC pinch-out at the local topography high created by the underlying MTC-5. See the location in Figure 9B.

Figure 10. (A) Shear strength degradation of carbonate oozes during cyclic T-bar penetrometer tests, modified from Gaudin and White (2009). The loss of strength is expressed as the ratio of the remoulded shear strength to the intact shear strength, experienced by different soils during cycles of remoulding for siliciclastic sediments and carbonate oozes of the offshore NW Australia. (B) Undrained shear strength measurements from the Ocean Drilling Program and Integrated Ocean Drilling Program. Nine type sites are chosen from the top 100 m below seabed sediment and are normally consolidated on active and passive margins. Active margin sites include offshore Japan (Site C0001), Cascadia (Site U1329), and two sites offshore Costa Rica (Sites 1039 and U1414). Passive margin sites include Amazon Fan (Site 942), Madeira abyssal plain (Site 951), New Jersey (Site 1073), Carolina Slope (Site 1054), and Exmouth Plateau and Kangaroo Syncline (ODP 762). The shear strength of the carbonate ooze in the Kangaroo

Syncline is lower than that of siliciclastic sediments on other passive margins, and that is significantly lower than that of siliciclastic sediments on active margins. Data sets for this figure are adopted from the global survey of Sawyer and DeVore (2015). Black and red dotted lines are the average undrained shear strength for passive and active margins, respectively.

Figure 11. Sketch diagrams illustrating the evolution of multi-stacked MTCs in Kangaroo Syncline. (A) Deposition of MTC-1 and subsequent undeformed sediments. Note that the accumulation of undeformed sediments has created a weak layer at the basal shear surface of MTC-1. (B) Deposition of MTC-2. Note that the buried MTC-1 has provided lithological constraints to the lower section of the younger MTC-2. The top surface of the MTC-2 has created accommodation. (C) Deposition of MTC-3. Note that MTC-3 has partially filled the accommodation space created by MTC-2, the remaining accommodation space has split the paleo-seabed into two distinct zones. (D) Deposition of MTC-4. Note that MTC-4 has different thickness trends in different zones created by MTC-3.

Figure 12. (A) Bathymetric map calculated on the basal shear surface of MTC-2, with contours at intervals of 60 ms. (B) Bathymetric map calculated on the basal shear surface of MTC-3, with contours at intervals of 50 ms. (C) Bathymetric map calculated on the basal shear surface of MTC-4, with contours at intervals of 100 ms. (D) Bathymetric map calculated on the basal shear surface of MTC-5, with contours at intervals of 100 ms.

Figure 13. The composite diagram of the MTCs thickness relationships, notes that the Y axis stands for thickness in time, and the X axis indicates the length in kilometres. Generally, younger MTCs thicken in areas where older MTCs are relatively thinner, and vice versa.

Acknowledgements

This research was supported by the Fundamental Research Funds for the Central Universities, China. The first author thanks the Natural Science Foundation of Shanghai (under Grant No. 23ZR1467800) and the State Key Laboratory of Marine Geology (under Grant No. MGZ202303) for their financial support. We thank Michael A. Clare, Wei Li and Song Jing for helpful discussions while preparing the manuscript. We acknowledge the value of the "open data" policy from Geoscience Australia (https://www.ga.gov.au/data-pubs) and thank them for providing the seismic reflection data. This study used the Willem 3D and the Willem 2D seismic surveys. The GEBCO_2021 bathymetry map is downloaded from https://www.ngdc.noaa.gov/maps/autogrid/. Data for the shear strength measurements are adopted from Supporting Information S1 of Sawyer and DeVore (2015), which can be downloaded from https://agupubs.onlinelibrary.wiley.com/doi/full/10.1002/2015GL066603.

References

Dott Jr, R., 1963, Dynamics of subaqueous gravity depositional processes: AAPG Bulletin, v. 47, no. 1, p. 104-128.

Nardin, T. R., Hein, F., Gorsline, D. S., and Edwards, B., 1979, A review of mass movement processes sediment and acoustic characteristics, and contrasts in slope and base-of-slope systems versus canyon-fan-basin floor systems.

Barber, P., 1988, The Exmouth Plateau deep water frontier: a case history.

Nemec, W., 1990, Aspects of sediment movement on steep delta slopes: Coarse-grained deltas, v. 10, p. 29-73.

Exon, N., Haq, B., and Von Rad, U., Exmouth Plateau revisited: scientific drilling and geological framework, *in* Proceedings Proceedings of the Ocean Drilling Program, Scientific Results1992, Volume 122, Ocean Drilling Program College Station, Tex, p. 3-20.

Haq, B. U., Boyd, R. L., Exon, N. F., and von Rad, U., 1992, 47. EVOLUTION OF THE CENTRAL EXMOUTH PLATEAU: A POST-DRILLING PERSPECTIVE1.

Palmer-Julson, A., and Rack, F., 1992, The relationship between sediment fabric and planktonic microfossil taphonomy: how do plankton skeletons become pelagic ooze?: Palaios, p. 167-177.

von Rad, U., Haq, B.U., et al., 1992, Proceedings of the Ocean Program, Scientific Results: Ocean Drilling Program, v. Leg 122.

Boyd, R., Williamson, P., and Haq, B., 1993, Seismic Stratigraphy and Passive‐Margin Evolution of the Southern Exmouth Plateau: Sequence Stratigraphy and Facies Associations, p. 579-603.

Rack, F. R., Bryant, W. R., and Julson, A. P., 1993, Microfabric and physical properties of deep-sea high latitude carbonate oozes, Carbonate Microfabrics, Springer, p. 129-147.

Keep, M., Powell, C. M., and Baillie, P., 1998, Neogene deformation of the North West Shelf, Australia.

Tindale, K., Newell, N., Keall, J., Smith, N., Purcell, P., and Purcell, R., 1998, Structural evolution and charge history of the Exmouth Sub-basin, northern Carnarvon Basin, Western Australia: The sedimentary basins of Western Australia, v. 2.

Nissen, S. E., Haskell, N. L., Steiner, C. T., and Coterill, K. L., 1999, Debris flow outrunner blocks, glide tracks, and pressure ridges identified on the Nigerian continental slope using 3-D seismic coherency: The Leading Edge, v. 18, no. 5, p. 595-599.

Piper, D. J., Cochonat, P., and Morrison, M. L., 1999, The sequence of events around the epicentre of the 1929 Grand Banks earthquake: initiation of debris flows and turbidity current inferred from sidescan sonar: Sedimentology, v. 46, no. 1, p. 79-97.

Tanaka, H., and Locat, J., 1999, A microstructural investigation of Osaka Bay clay: the impact of microfossils on its mechanical behaviour: Canadian Geotechnical Journal, v. 36, no. 3, p. 493-508.

Driscoll, N. W., Weissel, J. K., and Goff, J. A., 2000, Potential for large-scale submarine slope failure and tsunami generation along the US mid-Atlantic coast: Geology, v. 28, no. 5, p. 407-410.

Van Bemmel, P. P., and Pepper, R. E., 2000, Seismic signal processing method and apparatus for generating a cube of variance values, Google Patents.

Hull, J., and Griffiths, C., 2002, Sequence stratigraphic evolution of the Albian to Recent section of the Dampier Sub-basin, North West Shelf, Australia: PhD thesis 1999. University of Adelaide, Australia.

Longley, I., Buessenschuett, C., Clydsdale, L., Cubitt, C., Davis, R., Johnson, M., Marshall, N., Murray, A., Somerville, R., and Spry, T., The North West Shelf of Australia—a Woodside perspective, *in* Proceedings The Sedimentary Basins of Western Australia 3: Proceedings of the Petroleum Exploration Society of Australia Symposium, Perth2002, Pet. Explor. Soc. of Aust. Perth, p. 27-88.

Posamentier, H. W., and Kolla, V., 2003, Seismic geomorphology and stratigraphy of depositional elements in deep-water settings: Journal of sedimentary research, v. 73, no. 3, p. 367-388.

Sultan, N., Cochonat, P., Foucher, J., Mienert, J., Haflidason, H., and Sejrup, H., 2003, Effect of gas hydrates dissociation on seafloor slope stability, Submarine mass movements and their consequences, Springer, p. 103-111.

Volpi, V., Camerlenghi, A., Hillenbrand, C. D., Rebesco, M., and Ivaldi, R., 2003, Effects of biogenic silica on sediment compaction and slope stability on the Pacific margin of the Antarctic Peninsula: Basin Research, v. 15, no. 3, p. 339-363.

Bünz, S., Mienert, J., Bryn, P., and Berg, K., 2005, Fluid flow impact on slope failure from 3D seismic data: a case study in the Storegga Slide: Basin Research, v. 17, no. 1, p. 109-122.

Frey Martinez, J., Cartwright, J., and Hall, B., 2005, 3D seismic interpretation of slump complexes: examples from the continental margin of Israel: Basin Research, v. 17, no. 1, p. 83-108.

Gee, M., Gawthorpe, R., and Friedmann, J., 2005, Giant striations at the base of a submarine landslide: Marine Geology, v. 214, no. 1-3, p. 287-294.

Kvalstad, T. J., Andresen, L., Forsberg, C. F., Berg, K., Bryn, P., and Wangen, M., 2005, The Storegga slide: evaluation of triggering sources and slide mechanics: Marine and Petroleum Geology, v. 22, no. 1, p. 245-256.

Solheim, A., Berg, K., Forsberg, C., and Bryn, P., 2005, The Storegga Slide complex: repetitive large scale sliding with similar cause and development: Marine and Petroleum Geology, v. 22, no. 1-2, p. 97-107.

Strout, J. M., and Tjelta, T. I., 2005, In situ pore pressures: What is their significance and how can they be reliably measured?: Marine and Petroleum Geology, v. 22, no. 1-2, p. 275-285.

Cathro, D. L., and Karner, G. D., 2006, Cretaceous–Tertiary inversion history of the Dampier Sub-Basin, Northwest Australia: insights from quantitative basin modelling: Marine and Petroleum Geology, v. 23, no. 4, p. 503-526.

Davies, R. J., and Clark, I. R., 2006, Submarine slope failure primed and triggered by silica and its diagenesis: Basin Research, v. 18, no. 3, p. 339-350.

Frey-Martínez, J., Cartwright, J., and James, D., 2006, Frontally confined versus frontally emergent submarine landslides: a 3D seismic characterisation: Marine and Petroleum Geology, v. 23, no. 5, p. 585-604.

Masson, D., Harbitz, C., Wynn, R., Pedersen, G., and Løvholt, F., 2006, Submarine landslides: processes, triggers and hazard prediction: Philosophical Transactions of the Royal Society A: Mathematical, Physical and Engineering Sciences, v. 364, no. 1845, p. 2009-2039.

Moscardelli, L., Wood, L., and Mann, P., 2006, Mass-transport complexes and associated processes in the offshore area of Trinidad and Venezuela: AAPG bulletin, v. 90, no. 7, p. 1059-1088.

Bull, S., Cartwright, J., and Huuse, M., 2009, A review of kinematic indicators from mass-transport complexes using 3D seismic data: Marine and Petroleum Geology, v. 26, no. 7, p. 1132-1151.

Gaudin, C., and White, D., 2009, New centrifuge modelling techniques for investigating seabed pipeline behaviour.

Sawyer, D. E., Flemings, P. B., Dugan, B., and Germaine, J. T., 2009, Retrogressive failures recorded in mass transport deposits in the Ursa Basin, Northern Gulf of Mexico: Journal of Geophysical Research: Solid Earth, v. 114, no. B10.

Masson, D., Wynn, R., and Talling, P., 2010, Large landslides on passive continental margins: processes, hypotheses and outstanding questions, Submarine mass movements and their consequences, Springer, p. 153-165.

Nelson, C. H., Escutia, C., Damuth, J. E., and Twichell, D., 2011, Interplay of mass-transport and turbidite-system deposits in different active tectonic and passive continental margin settings: external and local controlling factors: Sediment. Geol, v. 96, p. 39-66.

Posamentier, H. W., and Martinsen, O. J., 2011, The character and genesis of submarine mass-transport deposits: insights from outcrop and 3D seismic data: Mass-transport deposits in deepwater settings: Society for Sedimentary Geology (SEPM) Special Publication 96, p. 7-38.

Berndt, C., Costa, S., Canals, M., Camerlenghi, A., de Mol, B., and Saunders, M., 2012, Repeated slope failure linked to fluid migration: the Ana submarine landslide complex, Eivissa Channel, Western Mediterranean Sea: Earth and Planetary Science Letters, v. 319, p. 65-74.

Hengesh, J., Dirstein, J. K., and Stanley, A. J., 2012, Seafloor geomorphology and submarine landslide hazards along the continental slope in the Carnarvon Basin, Exmouth Plateau, North West Shelf, Australia: The APPEA Journal, v. 52, no. 1, p. 493-512.

Hansen, L., L'Heureux, J.-S., Sauvin, G., Polom, U., Lecomte, I., Vanneste, M., Longva, O., and Krawczyk, C. M., 2013, Effects of mass-wasting on the stratigraphic architecture of a fjord-valley fill: Correlation of onshore, shear-wave seismic and marine seismic data at Trondheim, Norway: Sedimentary Geology, v. 289, p. 1-18.

Hengesh, J., Dirstein, J., and Stanley, A., 2013, Landslide geomorphology along the Exmouth plateau continental margin, North West Shelf, Australia: Australian Geomechanics Journal, v. 48, no. 4, p. 71-92.

Olafiranye, K., Jackson, C. A.-L., and Hodgson, D. M., 2013, The role of tectonics and mass-transport complex emplacement on upper slope stratigraphic evolution: A 3D seismic case study from offshore Angola: Marine and Petroleum Geology, v. 44, p. 196-216.

Scarselli, N., McClay, K., and Elders, C., 2013, Submarine slide and slump complexes, Exmouth Plateau, NW Shelf of Australia, *in* Proceedings The Sedimentary Basins of Western Australia IV: Proceedings of the Petroleum Exploration Society of Australia Symposium, Perth, WA2013, Volume 18.

Harbitz, C. B., Løvholt, F., and Bungum, H., 2014, Submarine landslide tsunamis: how extreme and how likely?: Natural Hazards, v. 72, no. 3, p. 1341-1374.

Talling, P. J., CLARE, M. L., Urlaub, M., Pope, E., Hunt, J. E., and Watt, S. F., 2014, Large submarine landslides on continental slopes: geohazards, methane release, and climate change: Oceanography, v. 27, no. 2, p. 32-45.

Li, W., Alves, T. M., Wu, S., Völker, D., Zhao, F., Mi, L., and Kopf, A., 2015, Recurrent slope failure and submarine channel incision as key factors controlling reservoir potential in the South China Sea (Qiongdongnan Basin, South Hainan Island): Marine and Petroleum Geology, v. 64, p. 17-30.

Ortiz-Karpf, A., Hodgson, D., and McCaffrey, W., 2015, The role of mass-transport complexes in controlling channel avulsion and the subsequent sediment dispersal patterns on an active margin: the Magdalena Fan, offshore Colombia: Marine and Petroleum Geology, v. 64, p. 58-75.

Sawyer, D. E., and DeVore, J. R., 2015, Elevated shear strength of sediments on active margins: Evidence for seismic strengthening: Geophysical Research Letters, v. 42, no. 23, p. 10,216-210,221.

Urlaub, M., Talling, P. J., Zervos, A., and Masson, D., 2015, What causes large submarine landslides on low gradient (< 2°) continental slopes with slow (~ 0.15 m/kyr) sediment accumulation?: Journal of Geophysical Research: Solid Earth, v. 120, no. 10, p. 6722-6739.

Aqrawi, A. A., and Bø, T. H., 2016, Amplitude contrast seismic attribute, Google Patents.

Corella, J. P., Loizeau, J.-L., Kremer, K., Hilbe, M., Gerard, J., Le Dantec, N., Stark, N., González-Quijano, M., and Girardclos, S., 2016, The role of mass-transport deposits and turbidites in shaping modern lacustrine deepwater channels: Marine and Petroleum Geology, v. 77, p. 515-525.

DeVore, J. R., and Sawyer, D. E., 2016, Shear strength of siliciclastic sediments from passive and active margins (0–100 m below seafloor): insights into seismic strengthening, Submarine Mass Movements and their Consequences, Springer, p. 173-180.

Kneller, B., Dykstra, M., Fairweather, L., and Milana, J. P., 2016, Mass-transport and slope accommodation: Implications for turbidite sandstone reservoirs: AAPG Bulletin, v. 100, no. 2, p. 213-235.

Reis, A., Araújo, E., Silva, C., Cruz, A., Gorini, C., Droz, L., Migeon, S., Perovano, R., King, I., and Bache, F., 2016, Effects of a regional décollement level for gravity tectonics on late Neogene to recent large-scale slope instabilities in the Foz do Amazonas Basin, Brazil: Marine and Petroleum Geology, v. 75, p. 29-52.

Schnyder, J. S., Eberli, G. P., Kirby, J. T., Shi, F., Tehranirad, B., Mulder, T., Ducassou, E., Hebbeln, D., and Wintersteller, P., 2016, Tsunamis caused by submarine slope failures along western Great Bahama Bank: Scientific reports, v. 6, no. 1, p. 35925.

Ten Brink, U. S., Andrews, B. D., and Miller, N. C., 2016, Seismicity and sedimentation rate effects on submarine slope stability: Geology, v. 44, no. 7, p. 563-566.

Gavey, R., Carter, L., Liu, J. T., Talling, P. J., Hsu, R., Pope, E., and Evans, G., 2017, Frequent sediment density flows during 2006 to 2015, triggered by competing seismic and weather events: Observations from subsea cable breaks off southern Taiwan: Marine Geology, v. 384, p. 147-158.

Pope, E. L., Talling, P. J., Carter, L., Clare, M. A., and Hunt, J. E., 2017, Damaging sediment density flows triggered by tropical cyclones: Earth and Planetary Science Letters, v. 458, p. 161-169.

Nugraha, H. D., Jackson, C. A. L., Johnson, H. D., Hodgson, D. M., and Reeve, M. T., 2018, Tectonic and oceanographic process interactions archived in Late Cretaceous to Present deep‐marine stratigraphy on the Exmouth Plateau, offshore NW Australia: Basin Research.

Sobiesiak, M. S., Kneller, B., Alsop, G. I., and Milana, J. P., 2018, Styles of basal interaction beneath mass transport deposits: Marine and Petroleum Geology, v. 98, p. 629-639.

Sun, Q., Alves, T. M., Lu, X., Chen, C., and Xie, X., 2018, True volumes of slope failure estimated from a Quaternary mass‐transport deposit in the northern South China Sea: Geophysical Research Letters, v. 45, no. 6, p. 2642-2651.

Ward, N. I., Alves, T. M., and Blenkinsop, T. G., 2018, Submarine sediment routing over a blocky mass‐transport deposit in the Espírito Santo Basin, SE Brazil: Basin Research, v. 30, no. 4, p. 816-834.

Kioka, A., Schwestermann, T., Moernaut, J., Ikehara, K., Kanamatsu, T., McHugh, C., dos Santos Ferreira, C., Wiemer, G., Haghipour, N., and Kopf, A., 2019, Megathrust earthquake drives drastic organic carbon supply to the hadal trench: Scientific reports, v. 9, no. 1, p. 1553.

Lintern, D. G., Mosher, D., Moscardelli, L., Bobrowsky, P., Campbell, C., Chaytor, J., Clague, J., Georgiopoulou, A., Lajeunesse, P., and Normandeau, A., Subaqueous mass movements and their consequences: Assessing geohazards, environmental implications and economic significance of subaqueous landslides2019, Geological Society of London.

Omeru, T., and Cartwright, J. A., 2019, The efficacy of kinematic indicators in a complexly deformed mass transport deposit: insights from the deepwater Taranaki Basin, New Zealand: Marine and Petroleum Geology, v. 106, p. 74-87.

Paganoni, M., King, J. J., Foschi, M., Mellor-Jones, K., and Cartwright, J. A., 2019, A natural gas hydrate system on the Exmouth Plateau (NW shelf of Australia) sourced by thermogenic hydrocarbon leakage: Marine and Petroleum Geology, v. 99, p. 370-392.

Steventon, M. J., Jackson, C. A. L., Hodgson, D. M., and Johnson, H. D., 2019, Strain analysis of a seismically imaged mass‐transport complex, offshore Uruguay: Basin Research, v. 31, no. 3, p. 600-620.

Velayatham, T., Holford, S., Bunch, M., King, R., and Magee, C., 2019, 3D Seismic Analysis of Ancient Subsurface Fluid Flow in the Exmouth Plateau, Offshore Western Australia.

Watkinson, I. M., and Hall, R., 2019, Impact of communal irrigation on the 2018 Palu earthquake-triggered landslides: Nature Geoscience, v. 12, no. 11, p. 940-945.

Barrett, R., Bellwald, B., Talling, P., Micallef, A., Gross, F., Berndt, C., Planke, S., Myklebust, R., and Krastel, S., 2021, Does retrogression always account for the large volume of submarine megaslides? Evidence to the contrary from the Tampen Slide, offshore Norway: Journal of Geophysical Research: Solid Earth, v. 126, no. 2, p. e2020JB020655.

Gatter, R., Clare, M., Kuhlmann, J., and Huhn, K., 2021, Characterisation of weak layers, physical controls on their global distribution and their role in submarine landslide formation: Earth-Science Reviews, v. 223, p. 103845.

Wu, N., Jackson, C. A.-L., Johnson, H. D., and Hodgson, D. M., 2021a, Lithological, petrophysical, and seal properties of mass-transport complexes, northern Gulf of Mexico: AAPG Bulletin, v. 105, no. 7, p. 1461-1489.

Wu, N., Jackson, C. A. L., Johnson, H. D., Hodgson, D. M., Clare, M. A., Nugraha, H. D., and Li, W., 2021b, The formation and implications of giant blocks and fluid escape structures in submarine lateral spreads: Basin Research.

Nugraha, H. D., Jackson, C. A.-L., Johnson, H. D., Hodgson, D. M., and Clare, M. A., 2022, Extreme erosion by submarine slides: Geology, v. 50, no. 10, p. 1130-1134.

Wu, N., Nugraha, H. D., Zhong, G., and Steventon, M. J., 2022, The role of mass - transport complexes in the initiation and evolution of submarine canyons: Sedimentology.

Wu, N., Jackson, C. A.-L., Clare, M. A., Hodgson, D. M., Nugraha, H. D., Steventon, M. J., and Zhong, G., 2023, Diagenetic priming of submarine landslides in ooze-rich substrates: Geology, v. 51, no. 1, p. 85-90.

Wu, N., Zhong, G., Niyazi, Y., Wang, B., Nugraha, H. D., and Steventon, M. J., 2024, Transformation of dense shelf water cascade into turbidity currents: Insights from high-resolution geophysical datasets: Earth and Planetary Science Letters, v. 626, p. 118547.

Figure 1

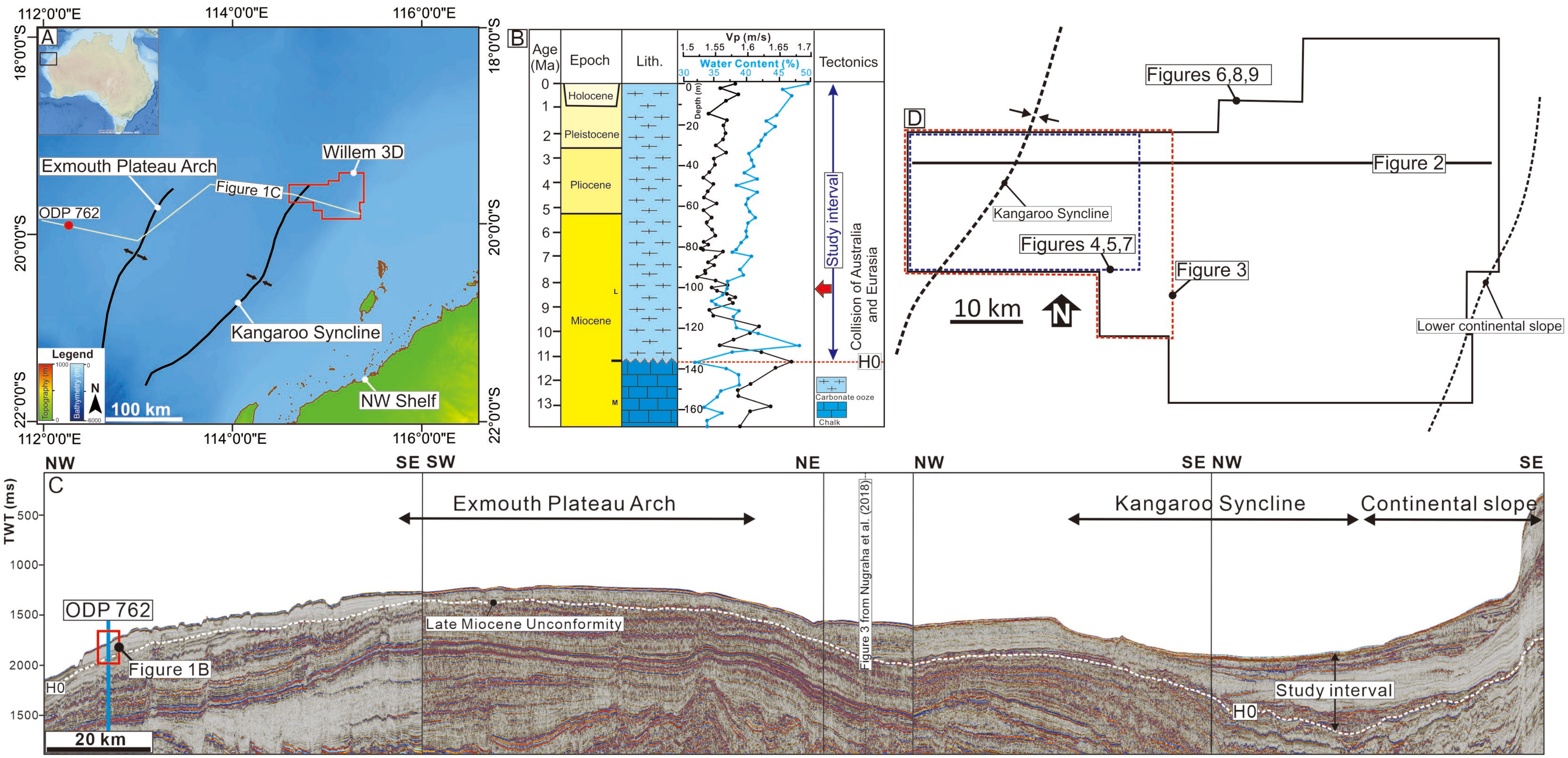

A
112°0'0"E
114°0'0"E
116°0'0"E
18°0'0"S
20°0'0"S
22°0'0"S
Willem 3D
Exmouth Plateau Arch
Figure 1C
ODP 762
Kangaroo Syncline
NW Shelf
Legend
100 km
B
Age (Ma)
Epoch
Lith.
Vp (m/s)
Water Content (%)
Tectonics
Holocene
Pleistocene
Pliocene
Miocene
Study interval
Collision of Australia and Eurasia
H0
Carbonate ooze
Chalk
D
Figures 6,8,9
Figure 2
Kangaroo Syncline
Figures 4,5,7
Figure 3
10 km
N
Lower continental slope
C
NW
SE SW
NE
NW
SE NW
SE
TWT (ms)
Exmouth Plateau Arch
Kangaroo Syncline
Continental slope
ODP 762
Figure 1B
Late Miocene Unconformity
Figure 3 from Nugraha et al. (2018)
Study interval
H0
20 km

Figure 2

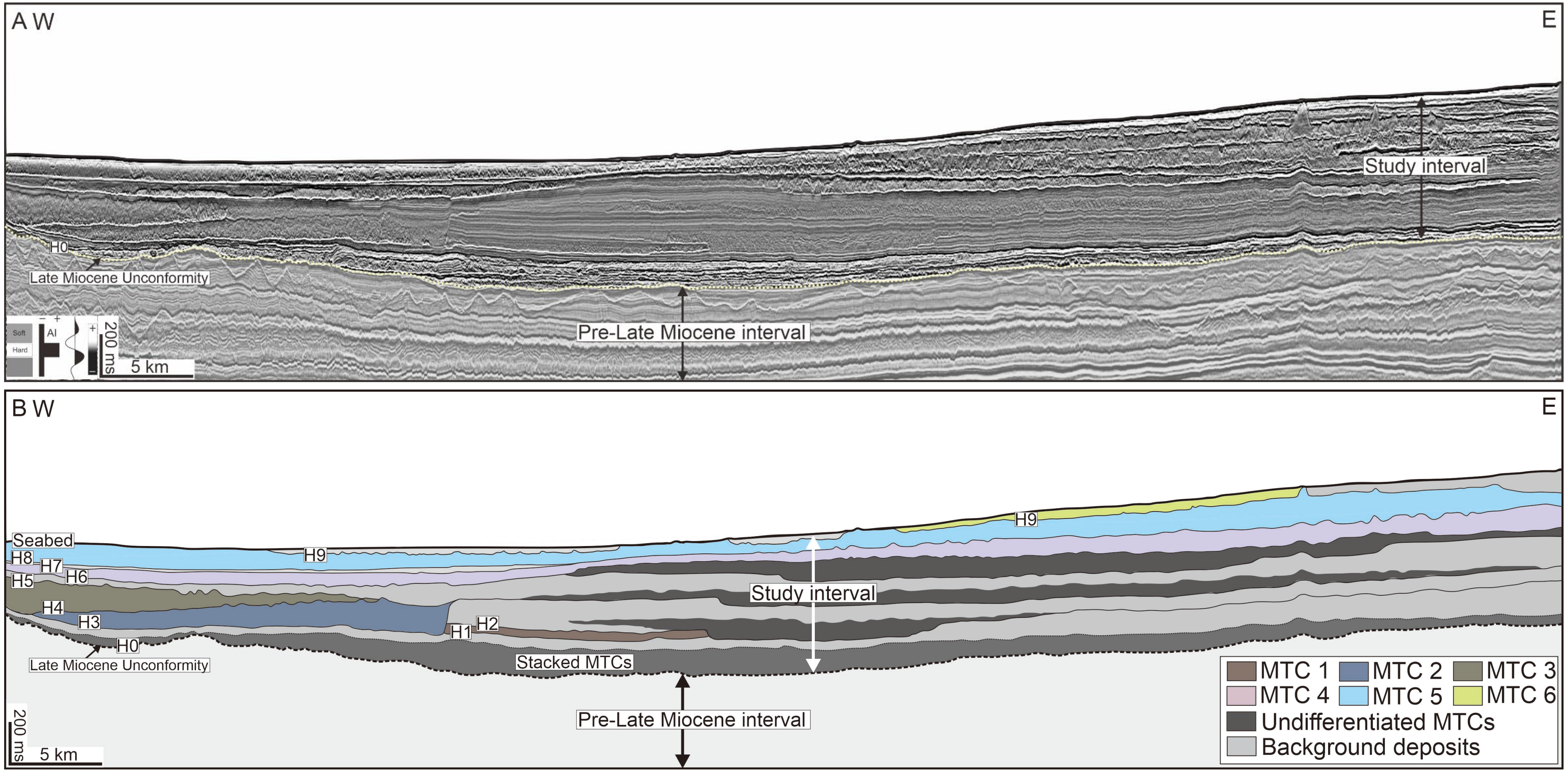

A W
E
Study interval
H0
Late Miocene Unconformity
Pre-Late Miocene interval
Soft
Hard
AI
200 ms
5 km
B W
E
Seabed
H8
H7
H6
H5
H4
H3
H9
H9
Study interval
H1
H2
H0
Late Miocene Unconformity
Stacked MTCs
Pre-Late Miocene interval
200 ms
5 km
MTC 1
MTC 2
MTC 3
MTC 4
MTC 5
MTC 6
Undifferentiated MTCs
Background deposits

Figure 3

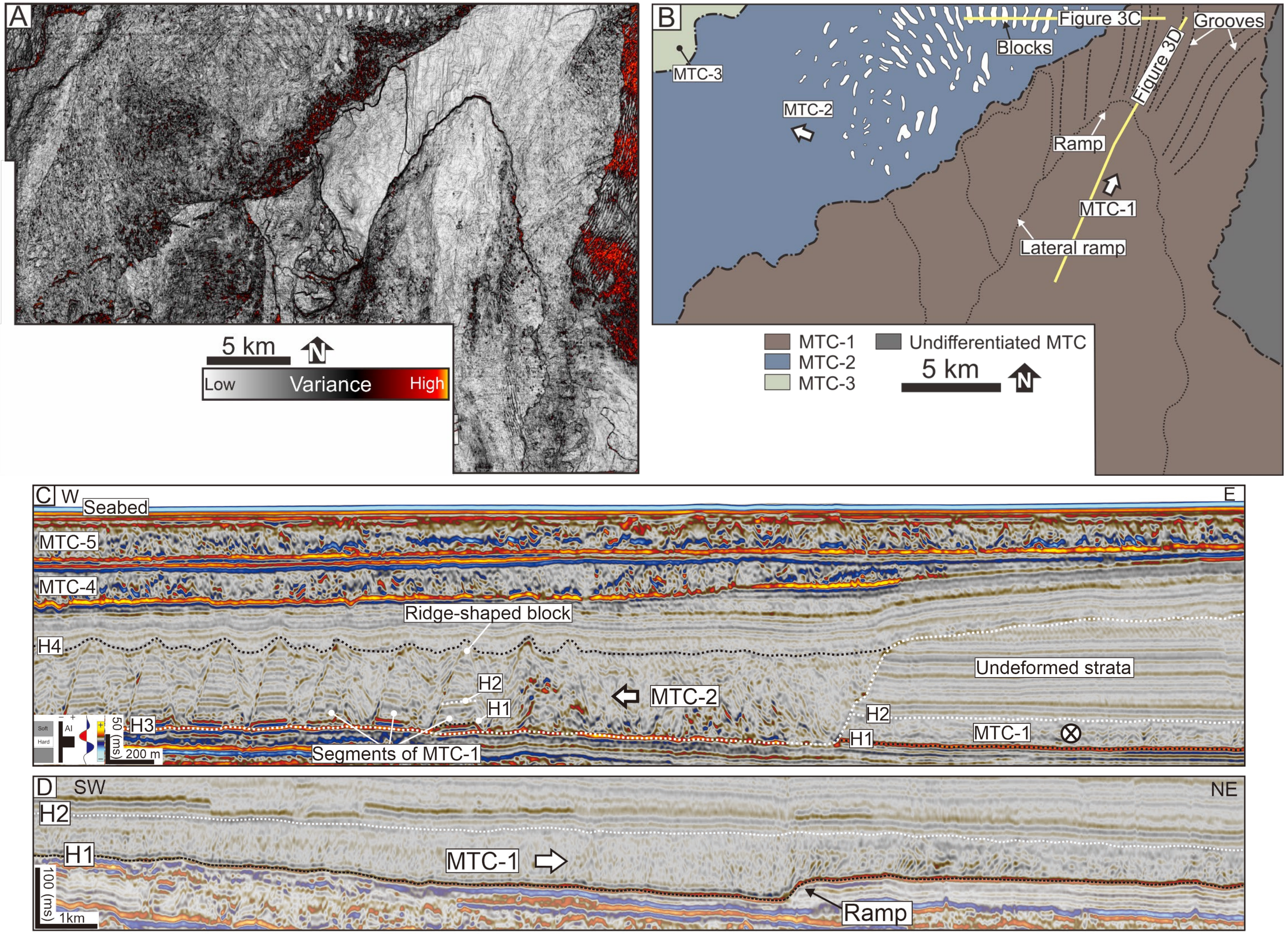
A
5 km
N
Low
Variance
High
B
MTC-3
MTC-2
Blocks
Figure 3C
Grooves
Figure 3D
Ramp
MTC-1
Lateral ramp
MTC-1
MTC-2
MTC-3
Undifferentiated MTC
5 km
N
C
W
E
Seabed
MTC-5
MTC-4
Ridge-shaped block
H4
Undeformed strata
H2
H1
MTC-2
H3
H2
H1
MTC-1
Segments of MTC-1
50 (ms)
200 m
D
SW
NE
H2
H1
MTC-1
100 (ms)
1km
Ramp

Figure 4

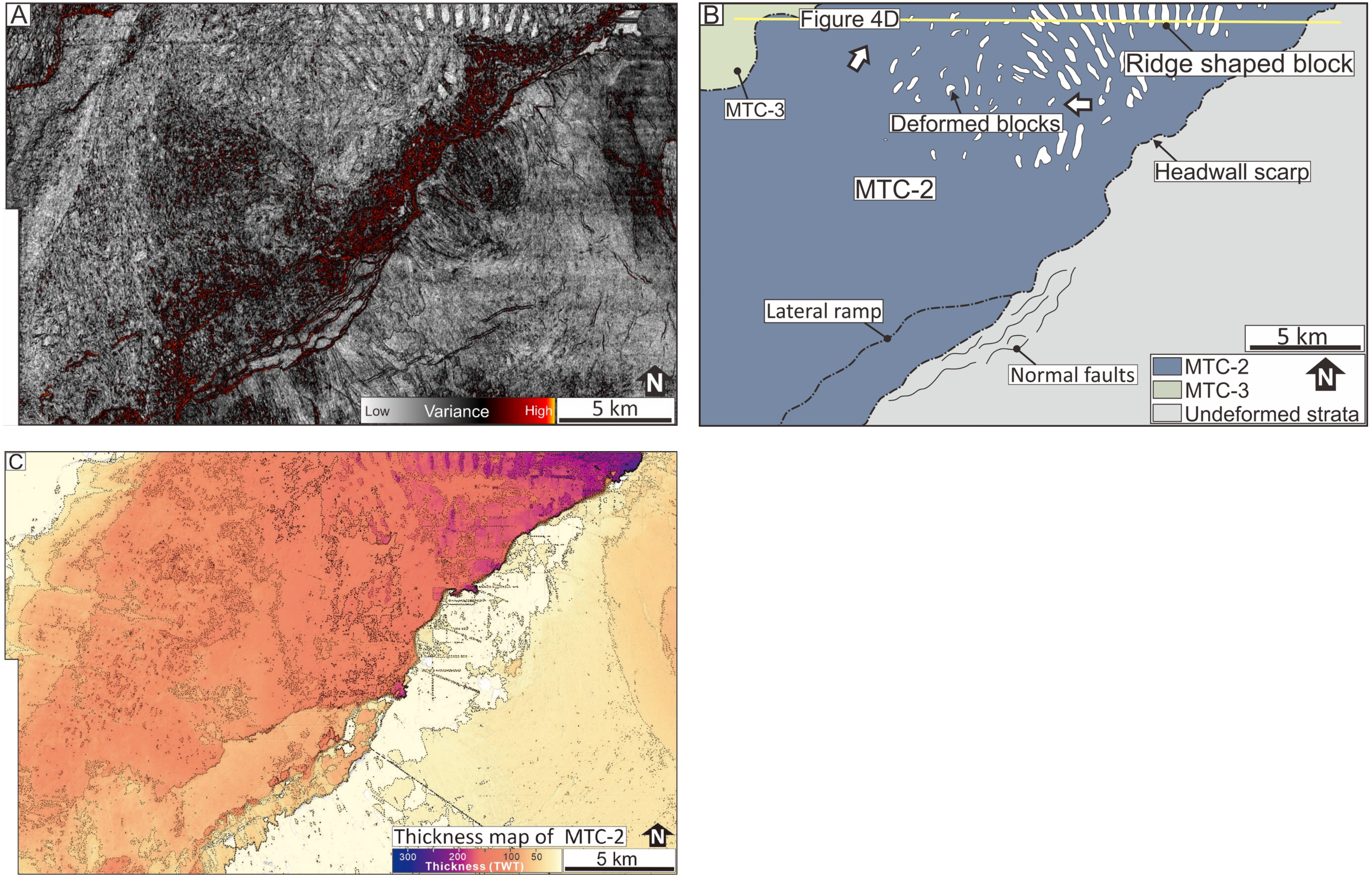

A
Low
Variance
High
5 km
N
B
Figure 4D
Ridge shaped block
MTC-3
Deformed blocks
Headwall scarp
MTC-2
Lateral ramp
5 km
Normal faults
MTC-2
MTC-3
Undeformed strata
N
C
Thickness map of MTC-2
300
200
100
50
Thickness (TWT)
5 km
N

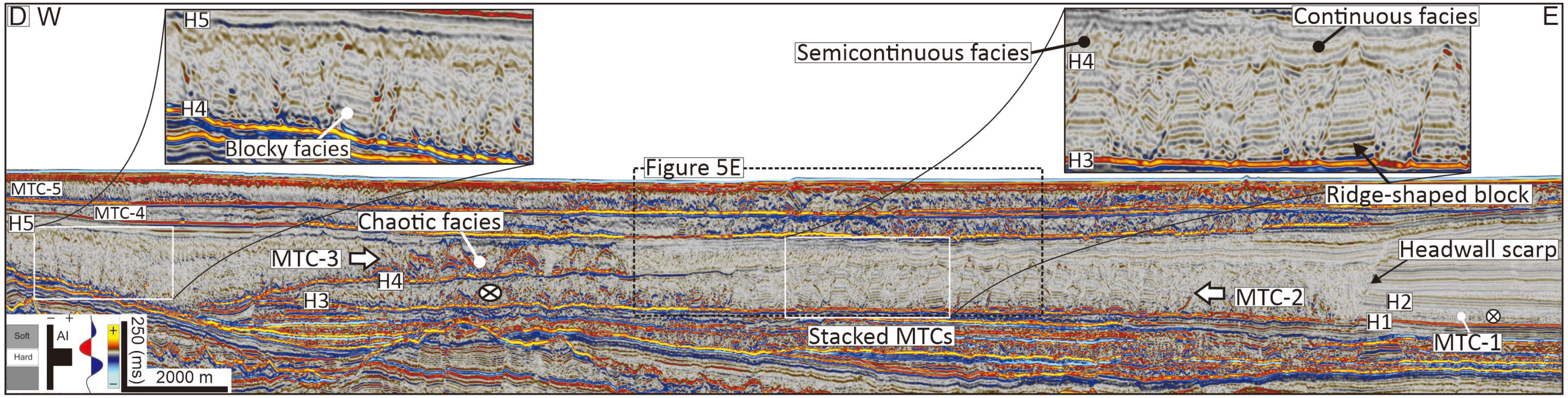
D
W
E
H5
H4
Blocky facies
Semicontinuous facies
Continuous facies
H4
H3
Figure 5E
Ridge-shaped block
MTC-5
MTC-4
H5
Chaotic facies
MTC-3
H4
H3
Headwall scarp
MTC-2
H2
H1
MTC-1
Stacked MTCs
Soft
Hard
AI
250 (ms)
2000 m

Figure 5

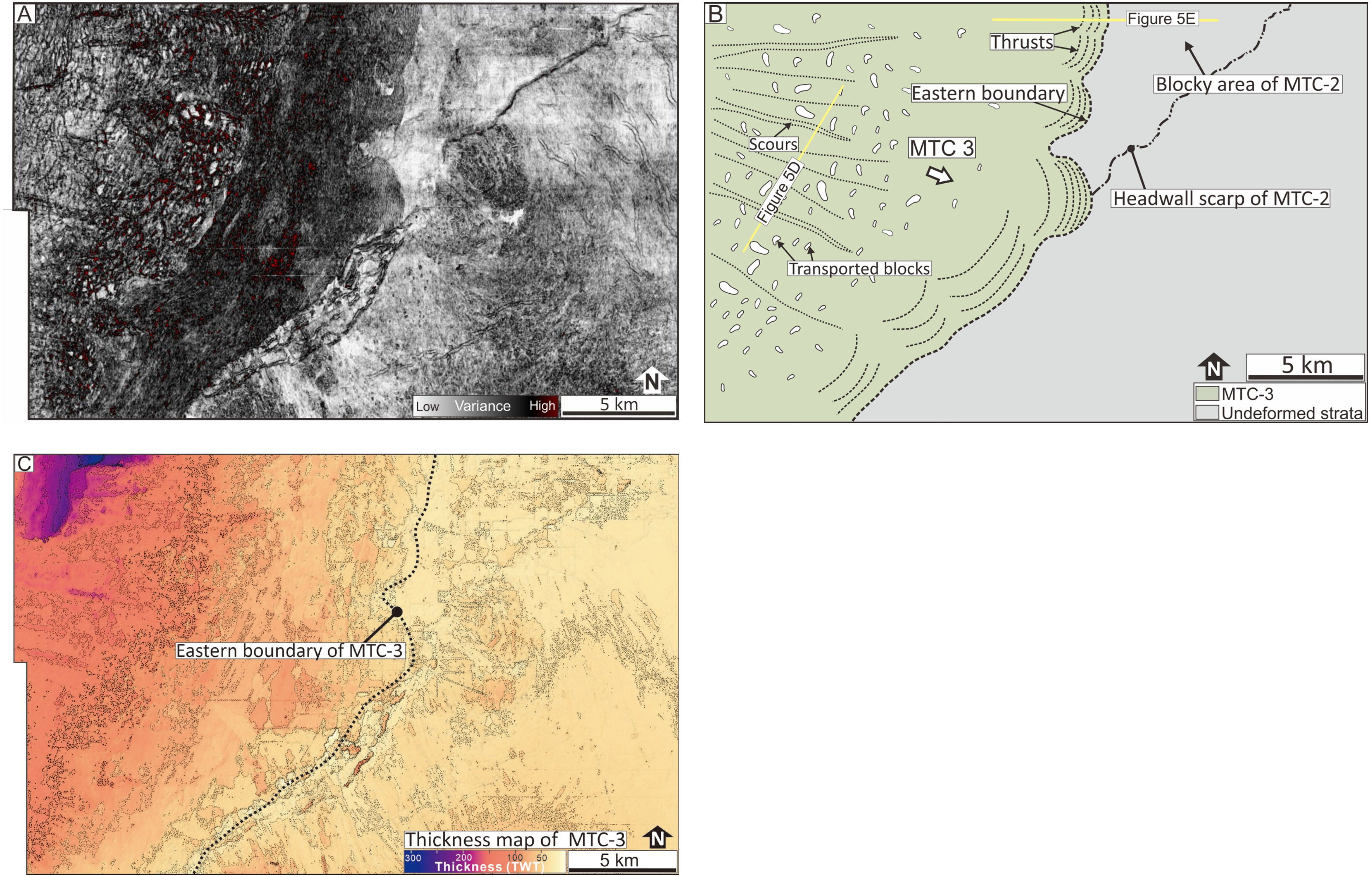

A
Low
Variance
High
5 km
N
B
Figure 5E
Thrusts
Blocky area of MTC-2
Eastern boundary
Scours
Figure 5D
MTC 3
Headwall scarp of MTC-2
Transported blocks
N
5 km
MTC-3
Undeformed strata
C
Eastern boundary of MTC-3
Thickness map of MTC-3
N
300
200
100
50
Thickness (TWT)
5 km

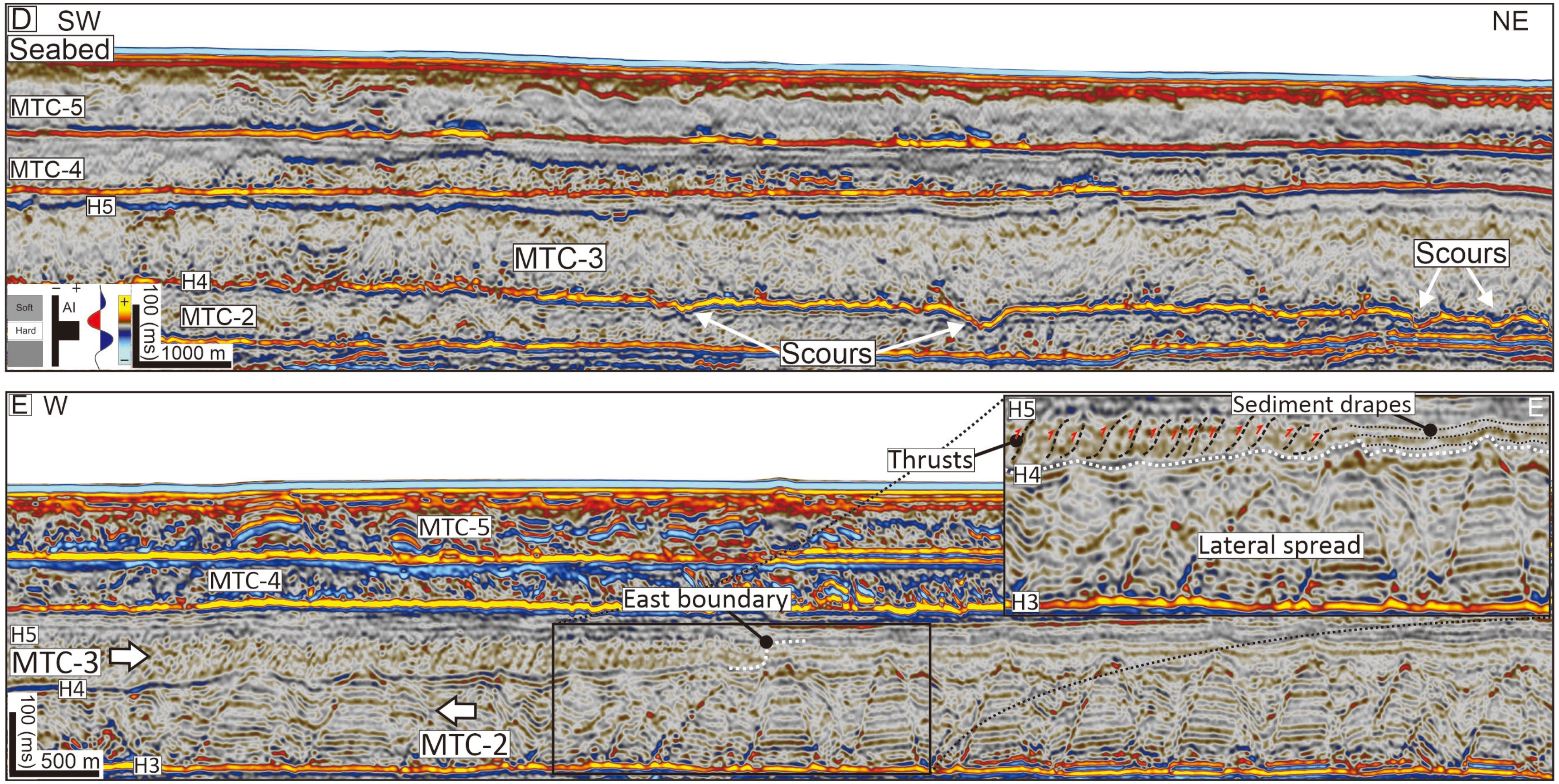
D
SW
NE
Seabed
MTC-5
MTC-4
H5
MTC-3
Scours
H4
MTC-2
Soft
Hard
AI
100 (ms)
1000 m
Scours
E
W
Thrusts
H5
Sediment drapes
E
H4
Lateral spread
H3
MTC-5
MTC-4
East boundary
H5
MTC-3
H4
MTC-2
100 (ms)
500 m
H3

Figure 6

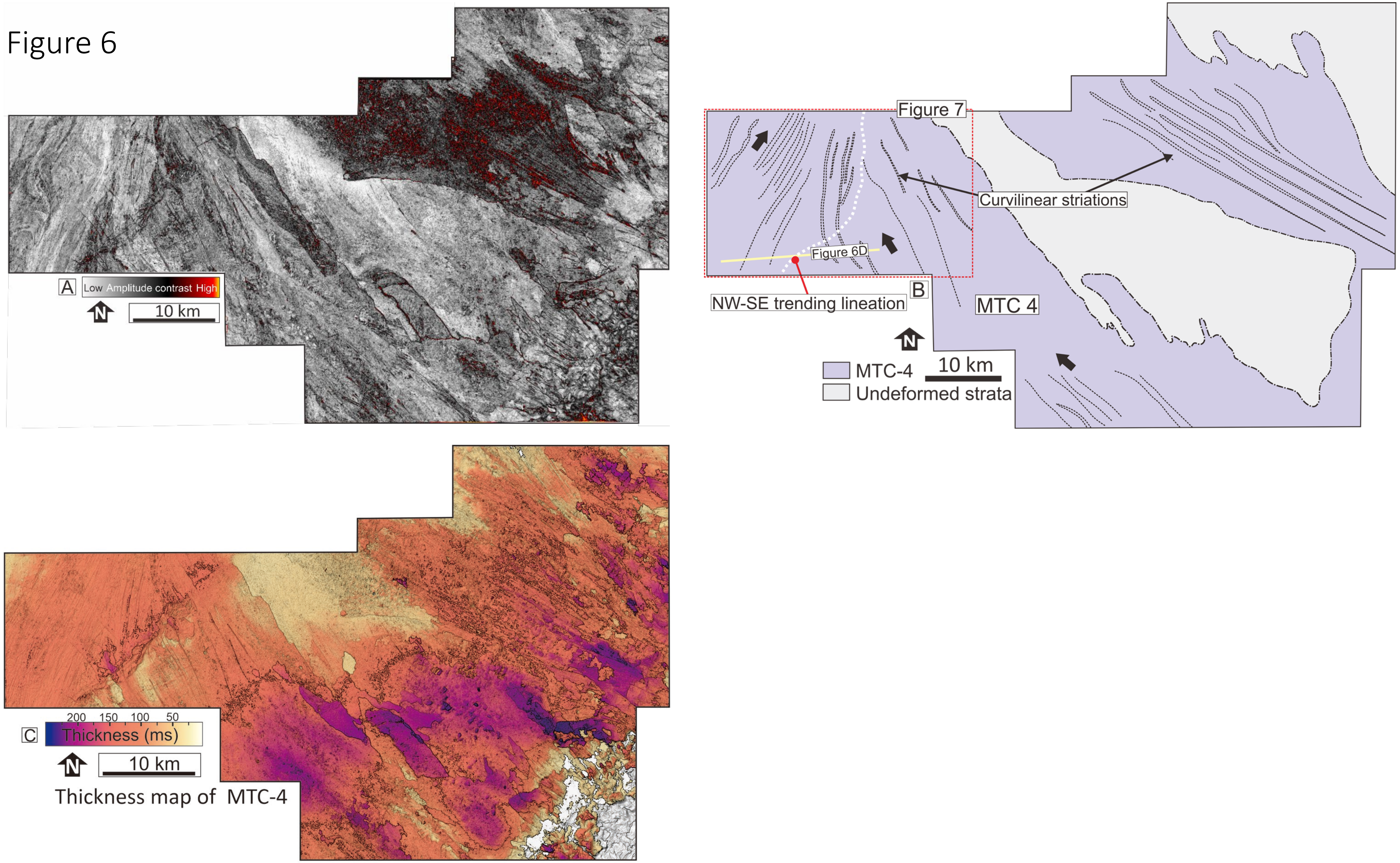
A
Low Amplitude contrast High
N
10 km
Figure 7
Curvilinear striations
Figure 6D
NW-SE trending lineation
B
MTC 4
N
MTC-4
10 km
Undeformed strata
200 150 100 50
C
Thickness (ms)
N
10 km
Thickness map of MTC-4

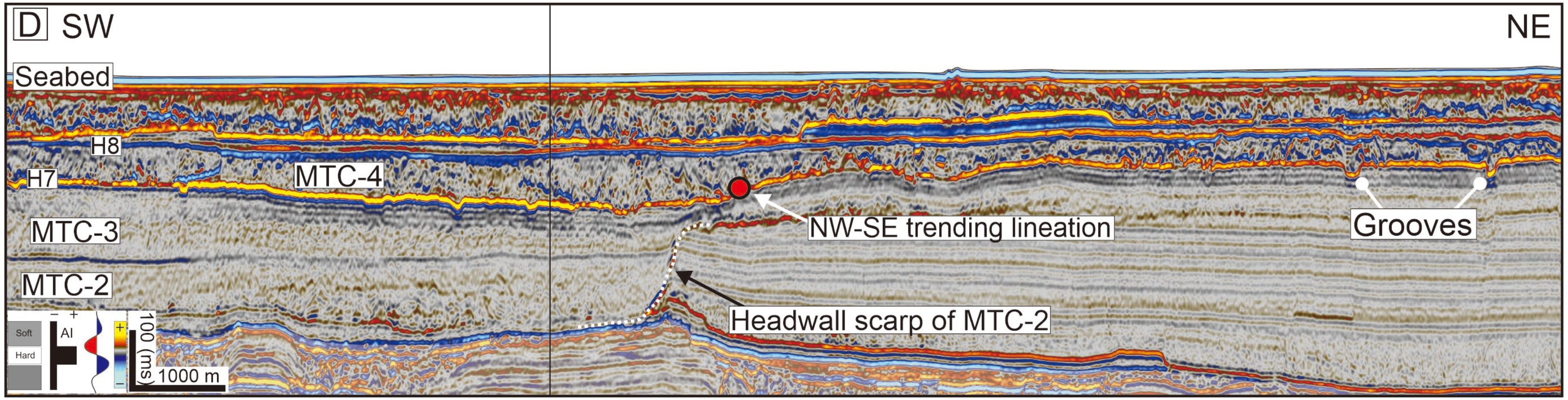

D
SW
NE
Seabed
H8
H7
MTC-4
MTC-3
MTC-2
NW-SE trending lineation
Grooves
Headwall scarp of MTC-2
Soft
Hard
AI
100 (ms)
1000 m

Figure 7

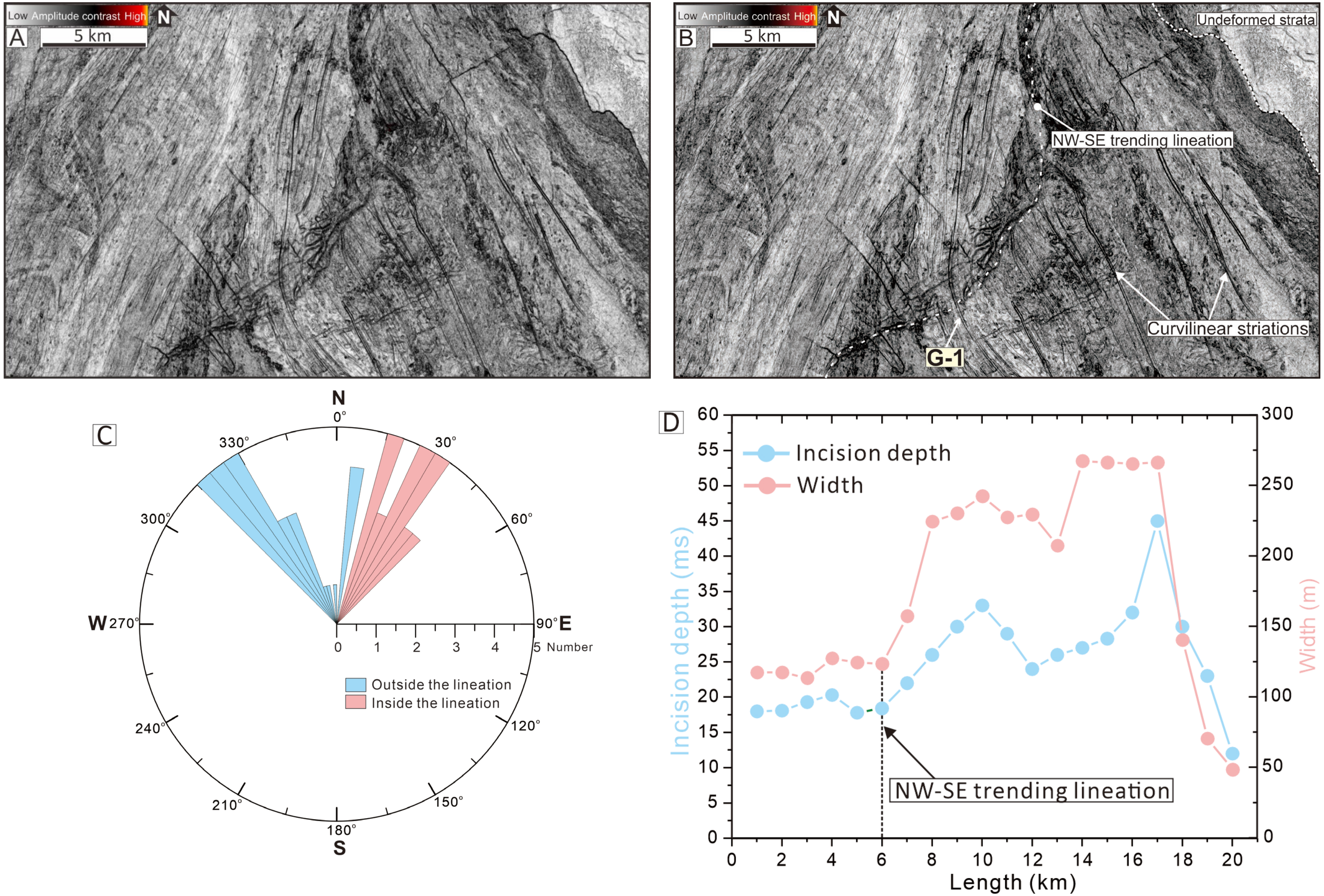

A
Low Amplitude contrast High
N
5 km
B
Low Amplitude contrast High
N
5 km
Undeformed strata
NW-SE trending lineation
Curvilinear striations
G-1
C
N
0°
30°
60°
90° E
120°
150°
180°
S
210°
240°
W 270°
300°
330°
0 1 2 3 4 5 Number
Outside the lineation
Inside the lineation
D
Incision depth
Width
Incision depth (ms)
Width (m)
Length (km)
NW-SE trending lineation

Figure 8

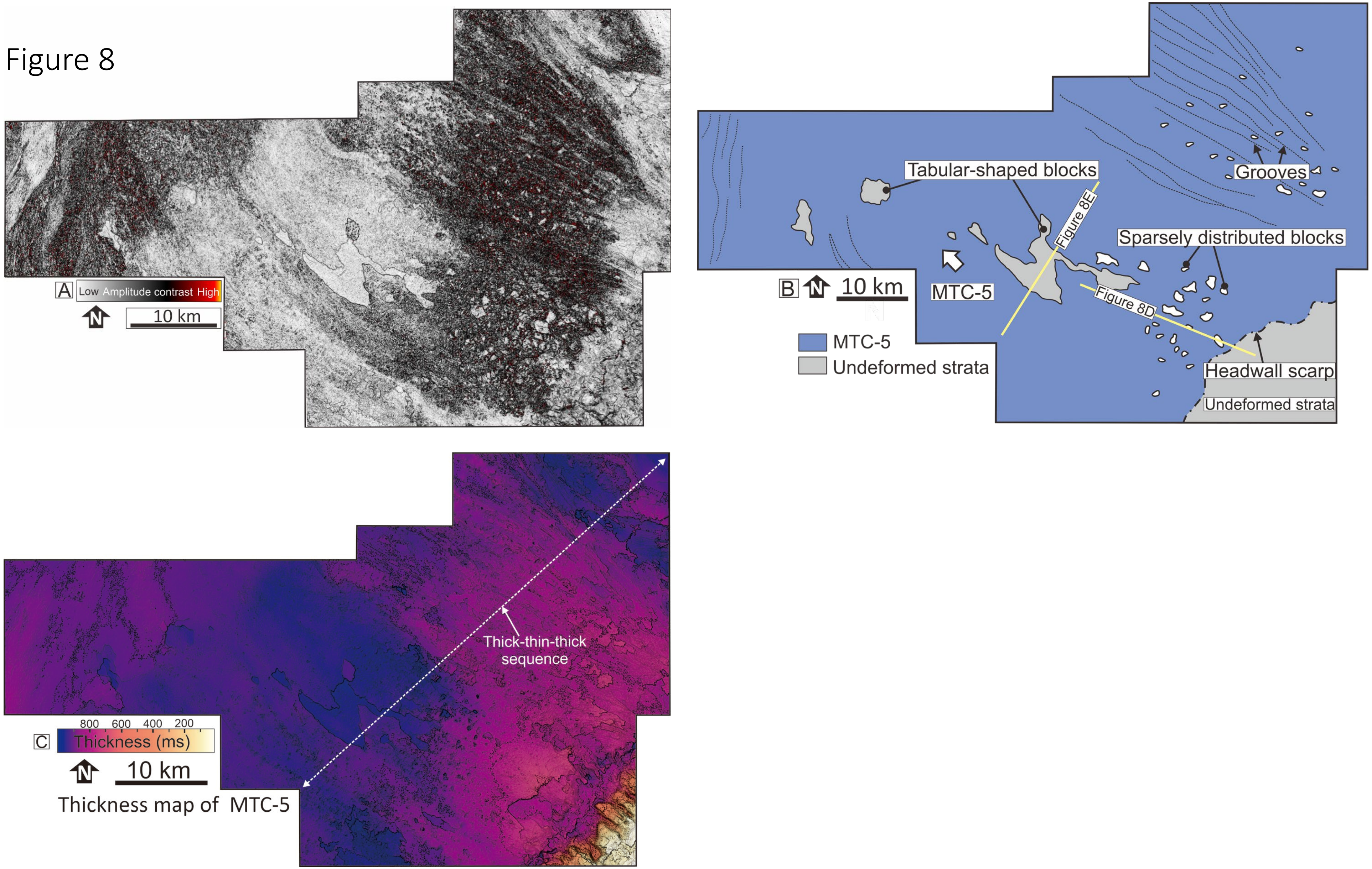

A
Low Amplitude contrast High
N
10 km
Tabular-shaped blocks
Grooves
Figure 8E
Sparsely distributed blocks
B
N
10 km
MTC-5
Figure 8D
MTC-5
Undeformed strata
Headwall scarp
Undeformed strata
Thick-thin-thick
sequence
800 600 400 200
C
Thickness (ms)
N
10 km
Thickness map of MTC-5

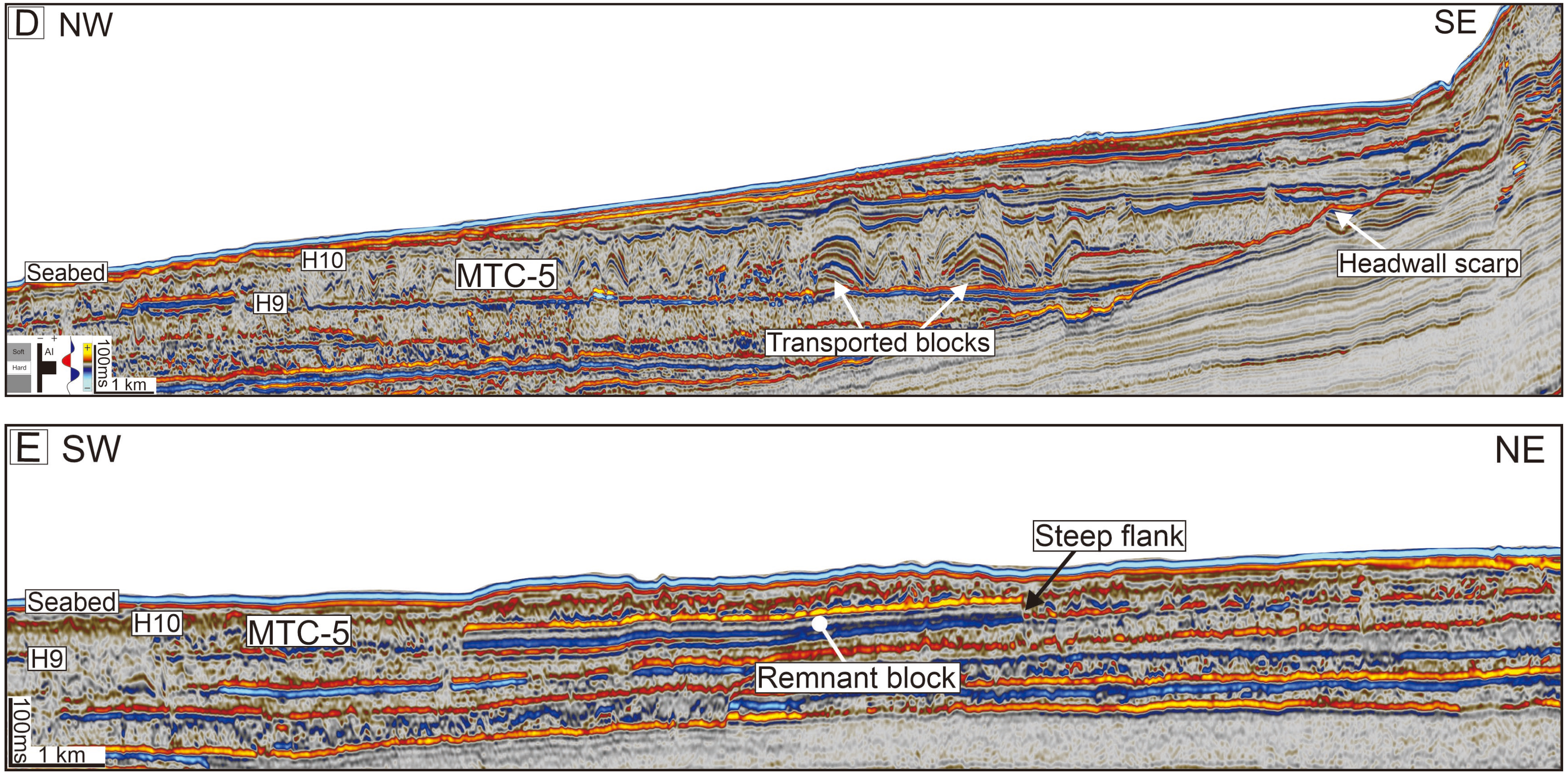

D
NW
SE
Seabed
H10
H9
MTC-5
Transported blocks
Headwall scarp
Soft
Hard
AI
100ms
1 km
E
SW
NE
Seabed
H10
H9
MTC-5
Remnant block
Steep flank
100ms
1 km

Figure 9

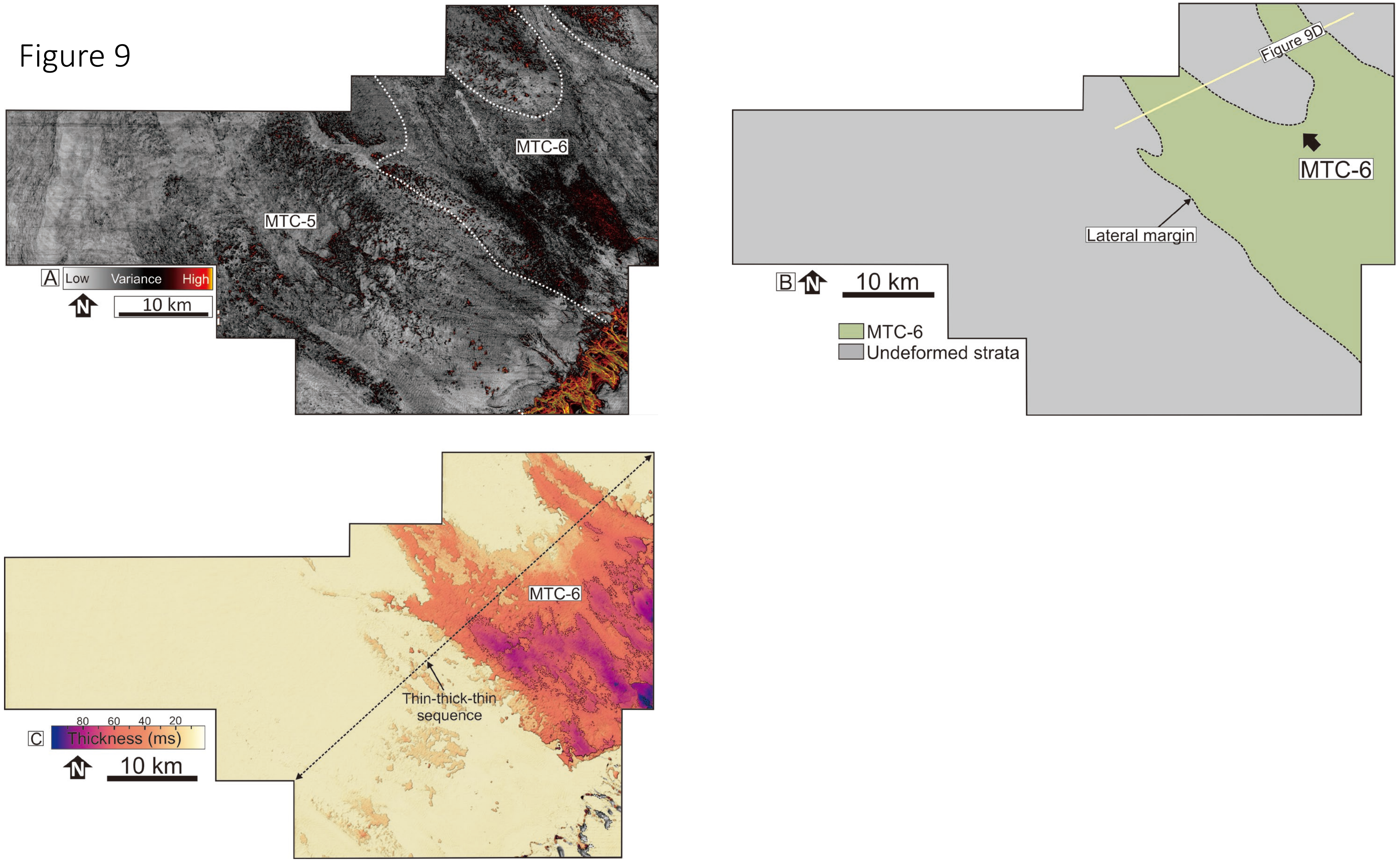
MTC-6
MTC-5
A
Low
Variance
High
10 km
Figure 9D
MTC-6
Lateral margin
B
10 km
MTC-6
Undeformed strata
MTC-6
Thin-thick-thin
sequence
C
80
60
40
20
Thickness (ms)
10 km

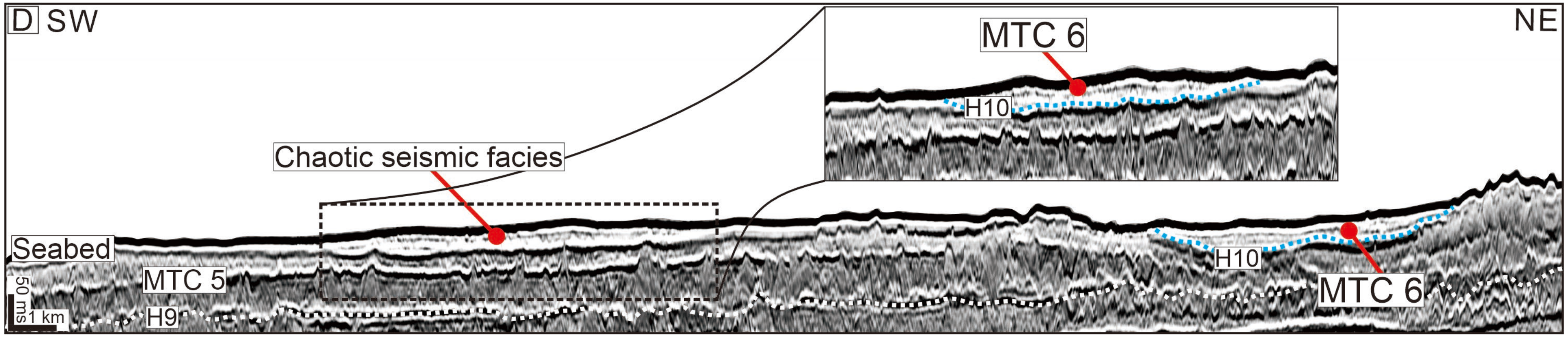
D
SW
NE
MTC 6
H10
Chaotic seismic facies
Seabed
MTC 5
50 ms
1 km
H9
H10
MTC 6

Figure 10

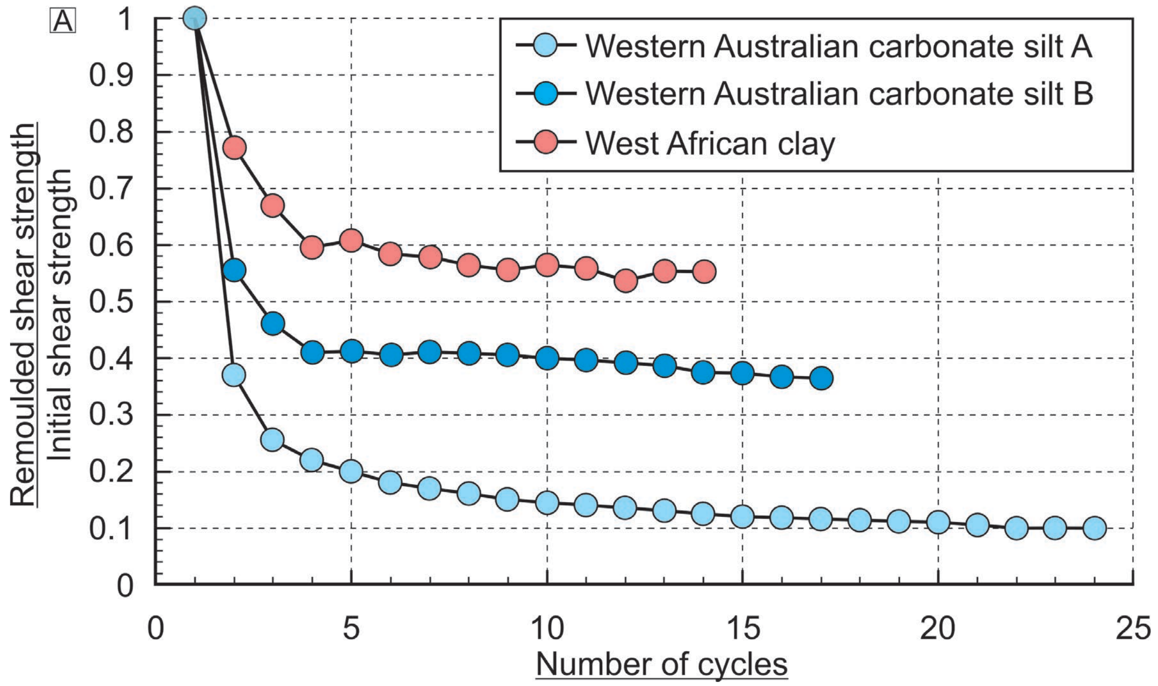

A
Remoulded shear strength / Initial shear strength
Number of cycles
Western Australian carbonate silt A
Western Australian carbonate silt B
West African clay

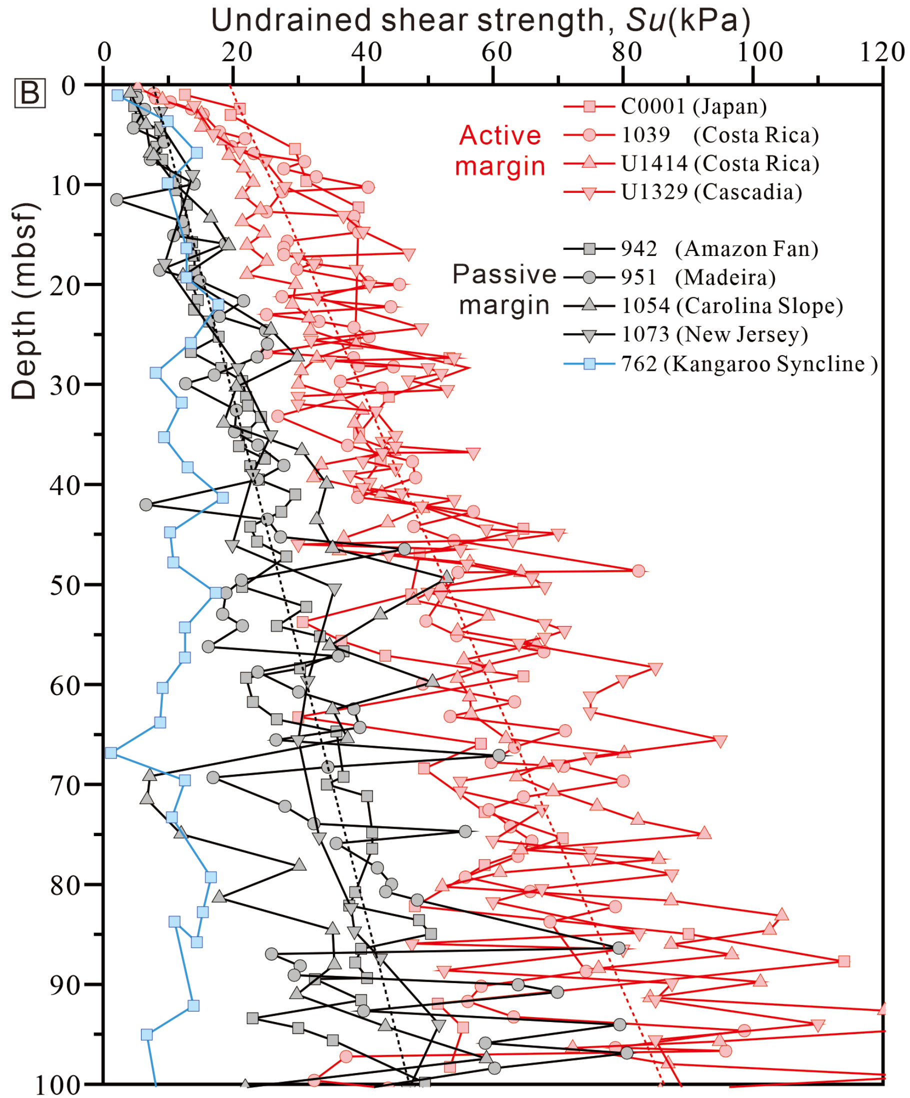

B
Undrained shear strength, Su(kPa)
Depth (mbsf)
Active margin
C0001 (Japan)
1039 (Costa Rica)
U1414 (Costa Rica)
U1329 (Cascadia)
Passive margin
942 (Amazon Fan)
951 (Madeira)
1054 (Carolina Slope)
1073 (New Jersey)
762 (Kangaroo Syncline)

Figure 11

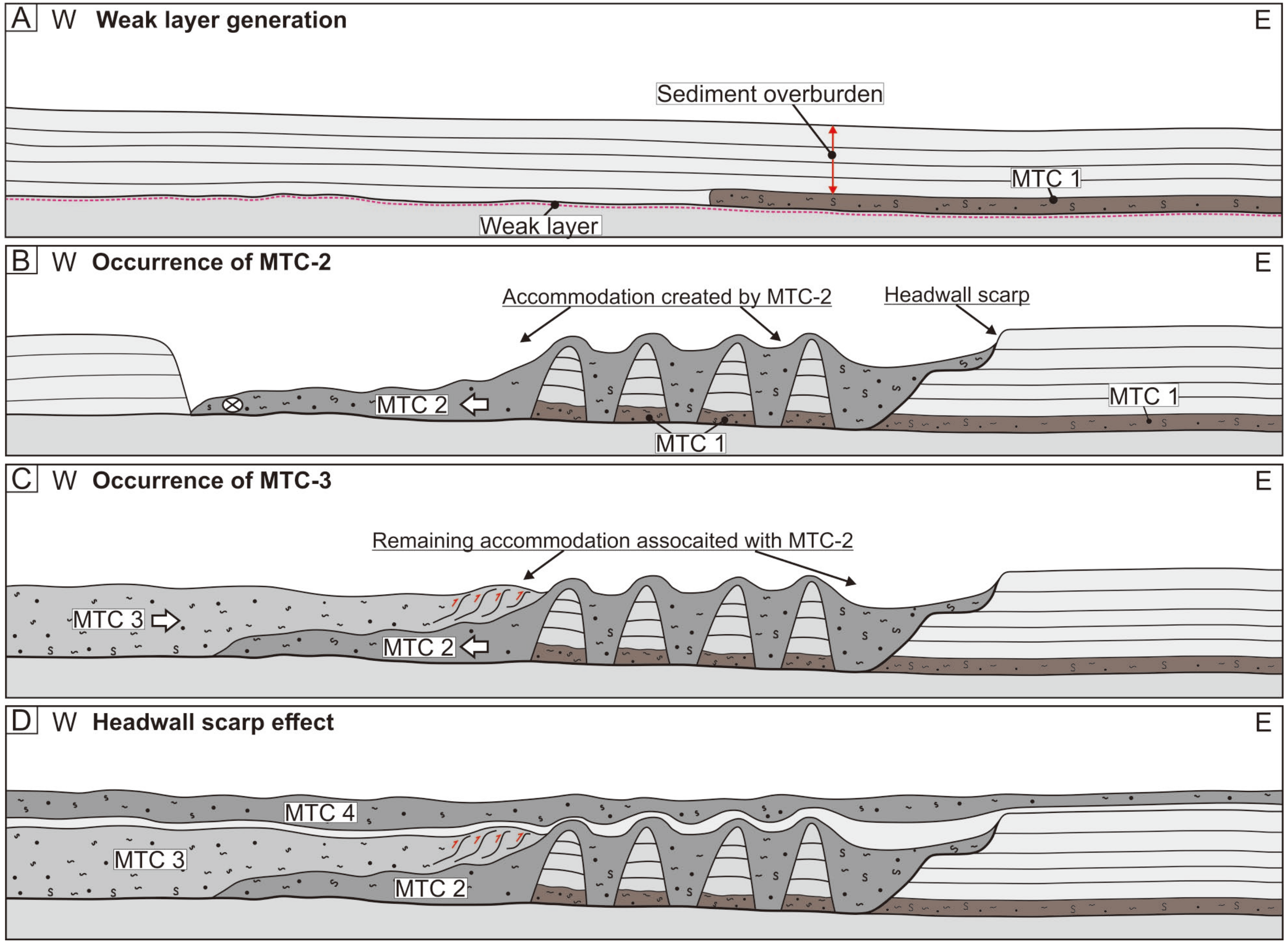

A
W
Weak layer generation
E
Sediment overburden
MTC 1
Weak layer
B
W
Occurrence of MTC-2
E
Accommodation created by MTC-2
Headwall scarp
MTC 2
MTC 1
MTC 1
C
W
Occurrence of MTC-3
E
Remaining accommodation assocaited with MTC-2
MTC 3
MTC 2
D
W
Headwall scarp effect
E
MTC 4
MTC 3
MTC 2

Figure 12

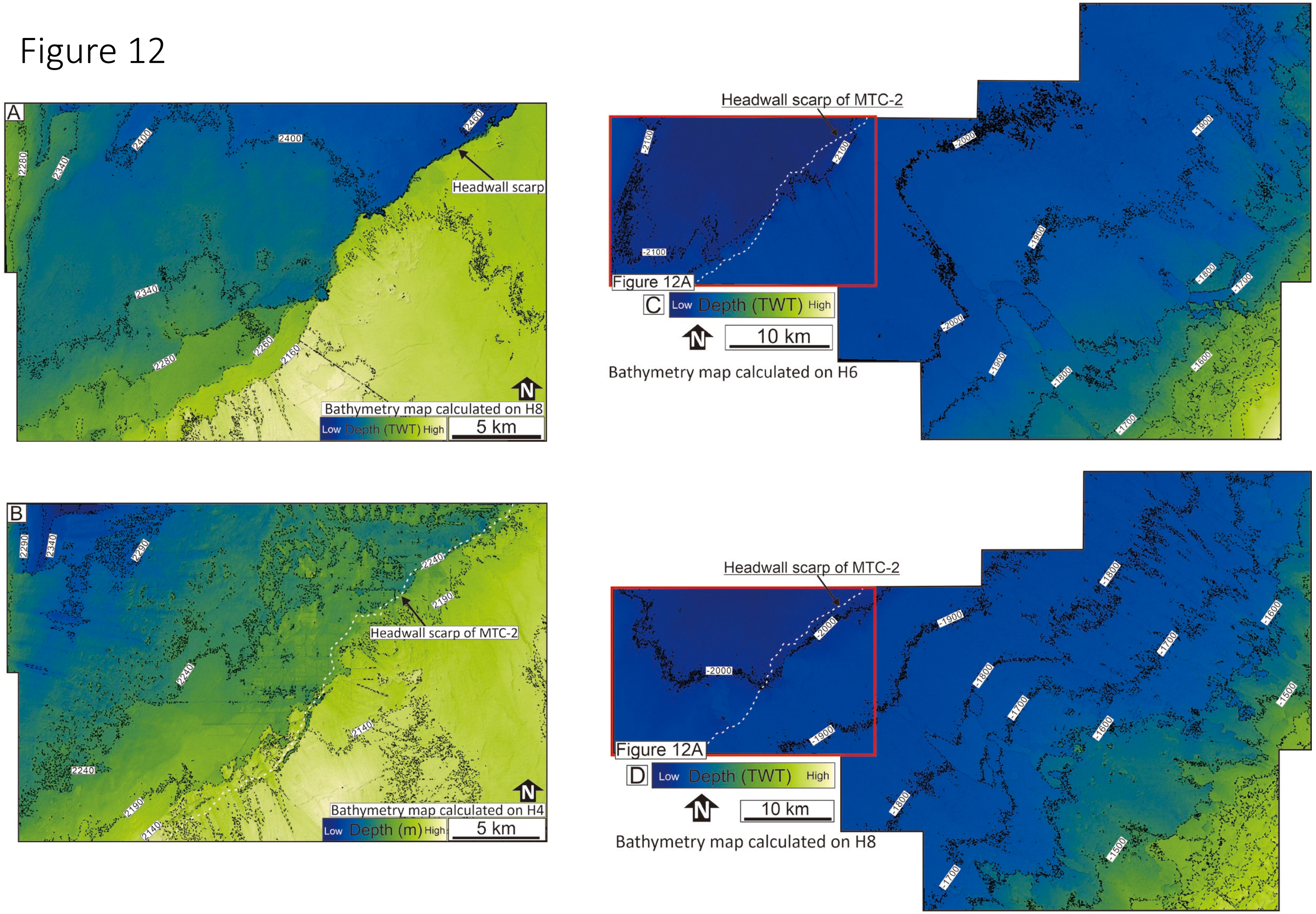

A
Headwall scarp
Bathymetry map calculated on H8
Low Depth (TWT) High
5 km
B
Headwall scarp of MTC-2
Bathymetry map calculated on H4
Low Depth (m) High
5 km
Headwall scarp of MTC-2
Figure 12A
C
Low Depth (TWT) High
10 km
Bathymetry map calculated on H6
Headwall scarp of MTC-2
Figure 12A
D
Low Depth (TWT) High
10 km
Bathymetry map calculated on H8

Figure 13

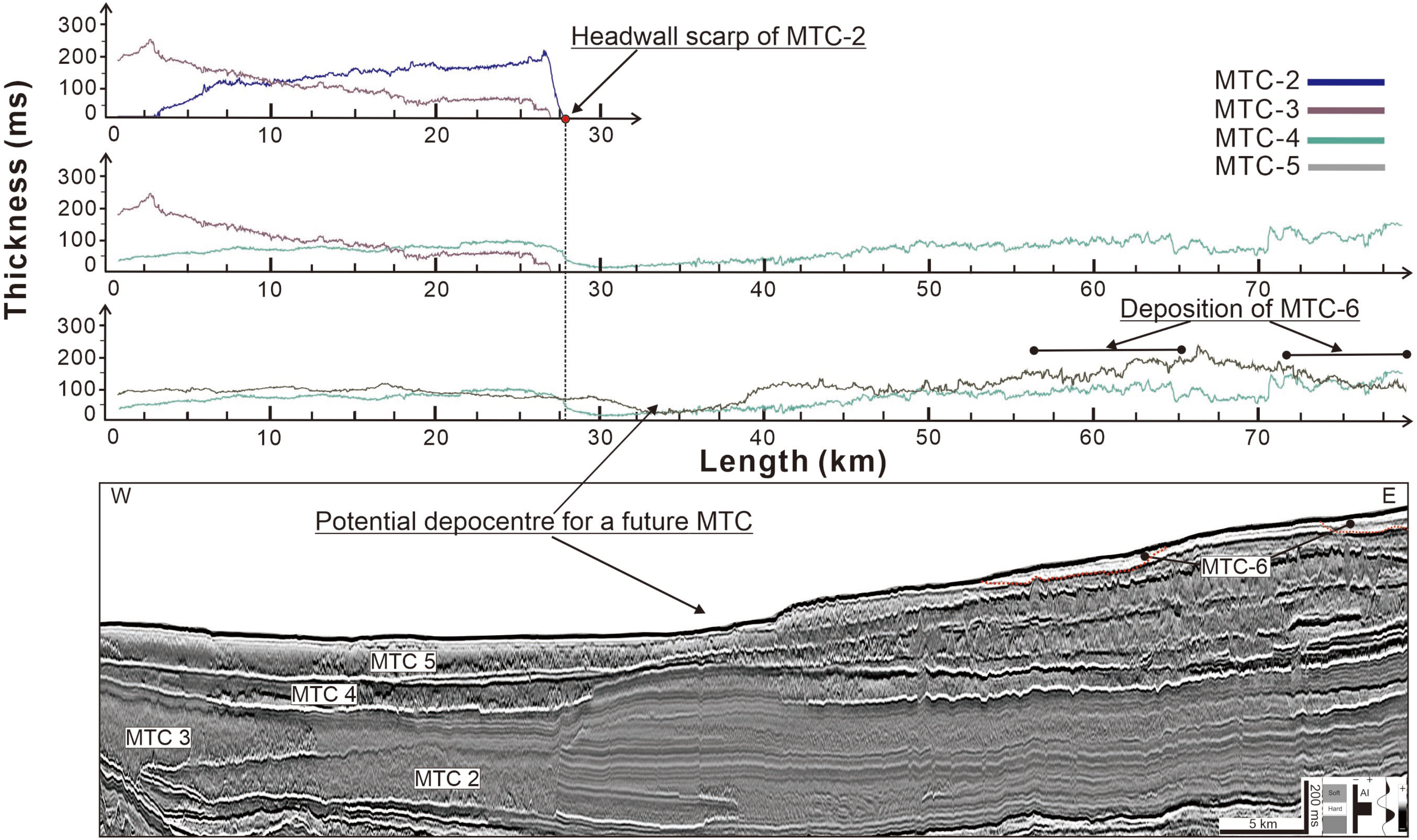

Headwall scarp of MTC-2
MTC-2
MTC-3
MTC-4
MTC-5
Thickness (ms)
Deposition of MTC-6
Length (km)
W
E
Potential depocentre for a future MTC
MTC-6
MTC 5
MTC 4
MTC 3
MTC 2
5 km
200 ms
Soft
Hard
AI